AN ABSTRACT OF THE THESIS OF

Daniel L. Caplan for the degree of Master of Science in Mechanical Engineering presented on March 20, 2020.

Title: Temperature Evolution of Nonreacting Spark Kernels at Sub-Atmospheric Pressures

Abstract approved: ____

David L. Blunck

In the event of a mid-flight flameout of a gas turbine engine, reignition is paramount to occupant safety. Ignition at high altitude can be challenging, due in part to the potentially lower ambient pressures. An understanding of the effects of sub-atmospheric pressures on the temperature evolution of spark kernels is needed to better understand the ignition process at high altitudes. Ultimately such information can be used to maximize ignition probability at high altitudes. The objective of this work was to determine the effects of decreasing pressure on the spatial and temperature evolution of spark kernels. Spark kernels were produced inside a vacuum chamber using a sunken fire igniter. An infrared camera was used to collect radiation intensity measurements from the spark kernels. An inverse deconvolution technique was employed to determine path-averaged temperatures from the radiation measurements. The technique determined temperatures using a narrow-band radiation emissions model (RADCAL). Temperatures determined using the technique agreed within 3% to temperature measurements using a thermocouple over a flat flame calibration burner.

Spark kernel temperatures were determined in quiescent air at absolute pressures from 300 to 1000 mbar. Kernel temperatures were measured from 0.67 to 4 ms after plasma was detected. Decreasing the ambient pressure caused an increase in average kernel temperature, and conversely a decrease in peak temperatures. For example, average kernel temperatures after 0.67

ms were 1270 K at 300 mbar, and 1125 K at 1000 mbar. Peak temperatures (i.e. the 90th percentile temperatures) were 2070 and 2360 K at 380 and 1000 mbar, respectively. Peak temperatures were hottest in a small region 0.6 igniter diameters from the igniter tip. Kernel temperatures decreased until the kernels became undetectable after 4 ms.

Electrical energy deposition and conversion efficiency to sensible energy decreased with decreasing pressure. For example, energy deposition decreased from 1.02 J at 1000 mbar to 0.85 J at 300 mbar, while conversion efficiency decreased from 80% to 30% at the same pressures. This pressure dependence of energy deposition and conversion efficiency is attributed to increased heat loss to the electrodes at decreased pressures due to lower breakdown voltage of air causing higher electrical current through the electrodes. The decrease in energy deposition and efficiency at lower pressure helps explain part of the challenge with achieving ignition at high altitude.

Kernel volume was independent of pressure. Kernels formed into a toroidal shape with an apparent volume of approximately 2.1 cubic igniter diameters (i.e., 3.7 cm^3) after 0.67 ms. The apparent kernel volume decreased approximately linearly over the kernels' lifetimes. Kernels penetrated faster and further from the igniter at lower pressures. For example, radiation from kernels at 1000 mbar was detected as far as 3 igniter diameters from the igniter tip, while at 300 mbar kernels were detected at least 3.4 diameters from the igniter tip. This observation is significant because the fuel-air mixture within combustors is not homogenous, hence the placement of the spark kernel within the flow is an important design consideration. The increased speed and penetration depth at lower pressure is attributed to an increased ratio of energy deposition to kernel mass due to the decreased gas density at lower pressure. The energy to mass ratio also explains the relationship between pressure and average kernel temperature.

Temperature Evolution of Nonreacting Spark Kernels at Sub-Atmospheric Pressures

by
Daniel L. Caplan

A THESIS

submitted to

Oregon State University

in partial fulfillment of
the requirements for the
degree of

Master of Science

Presented March 20, 2020
Commencement June 2020

Master of Science thesis of Daniel L. Caplan presented on March 20, 2020

APPROVED:

Major Professor, representing Mechanical Engineering

Head of the School of Mechanical, Industrial, and Manufacturing Engineering

Dean of the Graduate School

I understand that my thesis will become part of the permanent collection of Oregon State University libraries. My signature below authorizes release of my thesis to any reader upon request.

Daniel L. Caplan, Author

ACKNOWLEDGEMENTS

First and foremost, I would like to thank Dr. David Blunck for the opportunity to work on this research project. Without his advice, support, and never-ending patience, I would not be where I am today.

I would also like to thank the Air Force Research Laboratory for their invaluable assistance. In particular, I would like to thank Craig Neuroth for loaning the exciter and igniter, Scott Stouffer for his advice and coordination of the electrical energy deposition measurements, and Tyler Hendershott and Jen Colborn for performing the electrical measurements.

I would like to thank Oregon State University for funding, and Jonathan Bonebrake and Nathan Schorn of the OSU Propulsion Laboratory for use of the vacuum chamber.

Many thanks to Bryan Cmelak and Tyler Castile for your instrumental assistance in machining and data collection. I could not have done this without you.

To my lab mates in the Propulsion and CIRE Labs, thank you the fun times, adventures, and discussions. Because of you, I still have my sanity.

Finally, I would like to thank my friends and family for their support and patience through this journey. It’s been a long one, but worth it in the end.

TABLE OF CONTENTS

Page

TABLE OF CONTENTS (Continued)

LIST OF FIGURES

LIST OF FIGURES (Continued)

LIST OF FIGURES (Continued)

LIST OF TABLES

LIST OF SYMBOLS

Abbreviations

GTE	Gas turbine engine
IC	Internal combustion
IR	Infrared
MIE	Minimum Ignition Energy
PID	Proportional-integral-derivative
ROI	Region of interest
RSS	Square root of the sum of the squares

Symbols

I_λ	Infrared radiation intensity (spectral)
c_p	Constant pressure specific heat capacity
a	Area represented by each pixel
c	Air composition
D	Igniter diameter
E	Energy
h	Enthalpy
i	Current
I	Infrared radiation intensity
P	Pressure
r	Radial location relative to the igniter axis of symmetry
s	Line-of-sight path length
T	Temperature, or path averaged temperature
t	Time
V	Voltage or volume
z	Axial location relative to the igniter tip
α	Spectral transmissivity
κ	Absorption coefficient
ρ	Density
τ	Optical thickness
ϕ	Relative humidity
Φ	Equivalence ratio

Subscripts

0	Reference
∞	Ambient
avg	Average
b	Blackbody
g	Gas
i	Index representing each kernel image
k	Index representing each pixel within the kernel in an image
v	Vapor
λ	Wavelength

DEDICATION

I would like to dedicate this thesis to my wife, Ashley. Without her love, support, and enduring patience, I never would have been able to complete this monumental milestone.

Chapter 1 Introduction

1.1 Motivation

Ensuring reliable ignition in aviation gas turbine engines (GTEs) is imperative for safe operation. Reignition in the event of a mid-flight flameout is paramount to occupant safety. However, reignition at high altitude (e.g., 10,000 meters or 35,000 feet above sea level) can be challenging due in part to the lower ambient pressures and temperatures. Many aircraft cruise at altitudes above their reignition ceiling. If an aircraft's engine(s) flameout above the reignition ceiling, the aircraft must descend to a lower altitude before reignition can be accomplished.

Reliable reignition is of particular importance now. With the threat posed by climate change there is a push to move to alternative fuels and reduce emissions with leaner air-fuel ratios [1]. As GTEs are made to operate at these new conditions they approach extinction limits, increasing the likelihood of a lean flameout [1,2]. High altitude reignition may also become more challenging as the industry shifts toward leaner fuel-air ratios, more premixed combustors, and alternative fuels [1]. Designing an engine for ignition on alternative fuels in particular can be challenging due to the increased variability of the fuel chemistry and the limited data available about their performance [3,4].

Flameout can be caused by excessive ingestion of water or other contaminants into the engine core. The most common cause of excessive water ingestion is flying through storms. Modern weather radar is instrumental in helping pilots avoid flying through dangerous weather events. When storms are unavoidable, pilots are trained to operate the engines at a higher power setting [5]. Operating the engine at a higher power setting decreases the likelihood of a flameout. Operating at a higher power setting increases the centrifugal force of the main fan causing more water to be diverted to the bypass airflow. The increased flame strength in the combustor at higher power settings also increases the engine's ability to overcome water that enters into the core. However, avoiding storms and increasing throttle are both administrative safety controls that rely on pilot training and judgement and are not always followed. The Garuda International Flight GA421 crash in 2001 is a prime example of inadequate pilot training leading to catastrophic flameout of both engines [5,6]. The pilots of GA421 misinterpreted their onboard weather radar and failed to avoid an intense storm containing large amounts of rain and hail, which led to flameout of both turbofan engines within about 90 seconds of entering the storm. The pilots were unable to restart either engine and were forced to ditch the plane in a river [6]. While most occupants fortunately survived the incident, one member of the crew did not. There have also been incidents of engine flameouts after ingestion of volcanic ash which can be difficult to detect either visually or with onboard weather radar [7]. Incidents like these highlight the importance of reliable reignition at high altitude.

High altitude ignition is also required in augmenters for military aircraft. Augmenters, sometimes referred to as afterburners, are used to produce an on-demand increase in thrust [8]. Augmenters can be used during takeoff, or when a boost in speed is required mid-flight. Such an application requires rapid and reliable ignition both on the ground, and at high altitudes where the pressure at the inlet to the augmenter can be as low as 0.5 atm [8].

Several challenges exist in the ignition process of GTEs at high altitudes, as compared to low altitudes (e.g. on the ground). Some of these challenges include differences in thermodynamic properties, fluid mechanics, chemical kinetics, and electrical properties of air at high altitude. The cold air temperatures at high altitude increase the required energy to heat the fuel-air mixture to ignition temperature. The lower pressures can affect the fuel spray distribution and evaporation process [3]. The chemical kinetics of combustion are pressure dependent, and ignition at lower pressure is generally more challenging due increased mean free path between molecules [9]. The reduced pressure at high altitude also affects the dielectric breakdown voltage of air [10], which can alter the process by which electrical energy from an ignition system is converted to thermal energy.

When an ignition system produces a spark, it heats a small volume of gas called a spark kernel [1,9]. Ignition is successful when combustion occurring within the kernel propagates to consume the mixture surrounding the kernel. In order for this to happen, heat released by combustion must meet or exceed heat lost from the kernel. Heat can be lost from the kernel through conduction to the igniter electrodes, conduction to the surrounding fluid, radiation to the surrounding environment, and through evaporating fuel droplets within the kernel [1]. As a general rule, ignition is expected to be successful if a sufficiently sized volume of fuel-oxidizer mixture is heated to the adiabatic flame temperature of the mixture [1,9]. The energy required to heat that minimum volume of mixture to the flame temperature is the theoretical minimum ignition energy [1,9]. In practice, combustible mixtures can be ignited at temperatures significantly lower than their adiabatic flame temperatures, or conversely can fail to ignite when supplied with more than the theoretical minimum ignition energy. Part of this discrepancy may be due to the volumetric distribution of energy, and therefore temperatures, within the spark kernel.

Significant efforts have been made to study spark kernel temperatures in order to better understand the ignition process. Spark kernel temperature distributions have been calculated from schlieren imaged density gradients for kernels produced in nitrogen at atmospheric and elevated pressures [11–13]. Sforzo et al. reported isothermal spark kernel temperatures for kernels produced in air at stagnant and crossflow conditions at atmospheric pressure [14,15]. Blunck et al. and Okhovat et al. reported temperature distributions of spark kernels produced in air under quiescent and crossflow conditions, using an infrared thermography technique [16,17]. However, to the author's knowledge, measurements of spark kernel temperatures at sub-atmospheric pressures have not been attempted. Knowledge of spark kernel temperatures at sub-atmospheric pressures is needed to better understand how the ignition process can be altered by high altitude. Identifying this information can help engineers optimize the placement of igniters within combustion systems to maximize ignition performance at sub-atmospheric pressures.

1.2 Objectives

With this background and motivation in mind, the overall goal of this work is to quantify the effect of changes in pressure on the temperature and spatial evolution of spark kernels. Given the critical role that the temperature of a gas plays in the ignition process, this work focuses on the how decreasing pressure affects the conversion of electrical to thermal energy and the impacts on spark kernel temperatures. With these goals in mind, the objectives of this work are as follows:

I. Elucidate the effects of decreasing the pressure from atmospheric to sub-atmospheric on the spatial development of spark kernels.

II. Identify the effects of pressure on the distribution of temperatures within spark kernels.

III. Ascertain how decreasing the pressure alters the temperature evolution of spark kernels.

IV. Determine the impact of lowering pressure on the conversion of electrical energy to thermal energy in spark kernels.

It should be noted that this work is focused on energy conversion and thermal evolution of spark kernels, and is not focused on the process of ignition itself. It is anticipated that results from this work can be used by combustion researchers to gain a more complete understanding of spark ignition behavior, and by engineers when designing the selection and placement of igniters in combustors or augmenters.

Chapter 2 Literature Review

There are many different types of ignition sources used in combustion systems. Spark ignition is the most common form. Spark ignition is used in gas turbine engines (GTE) for both aviation and power generation, internal combustion (IC) engines in cars, generators, and propeller planes, as well as many types of burners used in industrial, commercial, and residential applications [9]. While many combustion devices, such as burners, operate at atmospheric pressure, some systems (usually engines) must be ignited at either high or low pressures. IC engines are an example of an application where reliable ignition is required at high pressures [18]. IC engines must ignite the mixture in each cylinder once every one or two revolutions of the crank (two stroke engines ignite every revolution, while four stroke engines ignite every other revolution). The speed and timing of ignition in an IC engine is of utmost importance; improper ignition timing can lead to poor combustion performance hurting efficiency and increasing harmful emissions [18]. Aviation gas turbine engines on the other hand must be capable of igniting at a range of pressures both above and below atmospheric pressure. Under normal conditions turbine engines require ignition only during start-up while on the ground, where pressure in the combustor is above ambient [3]. However, for safety reasons aviation GTEs are also required to be capable of reignition at high altitude, where pressure can be low [19].

Ignition prevention is another important consideration for some applications [20,21]. For example, non-pressurized aviation fuel tanks typically include an inlet vent that allows air to enter the tank while fuel is removed for consumption. This means that a potentially flammable mixture of air and fuel can exist inside the fuel tank [20–22], as was the case in the TWA 800 explosion [22]. Applications such as these require careful design to prevent dangerous accidents.

This chapter provides a discussion of spark ignition fundamentals, identifies the important factors affecting spark ignition, and provides a review of recent works on the topic. Particular emphasis is placed on the effects of pressure both directly and indirectly through the pressure dependence of other parameters.

2.1 Spark Ignition

2.1.1 Minimum Ignition Energy

Minimum ignition energy (MIE) is an often-used metric for predicting the ignitability of a fuel-air mixture. MIE is useful for designing ignition systems to maximize ignition probability or for safety systems with the goal of preventing ignition. MIE is an experimentally determined value that is dependent on many factors such as fuel chemistry, pressure, temperature, crossflow velocity, and the type of ignition source. The required ignition energy is dependent on the fuel-air ratio, and typically has a minimum value when mixtures are fuel-rich [23]. The resulting energy requirement curve will be 'U' shaped as shown in Figure 1. For applications where the goal is ignition prevention, the MIE is considered to be the minimum of this curve [24,25].

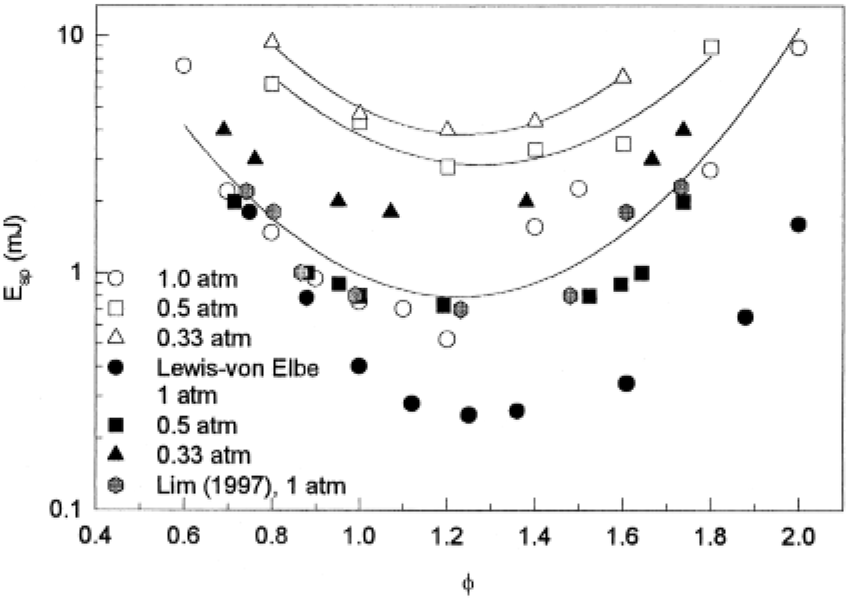

Figure 1 Minimum ignition energy for propane-air mixtures at various equivalence ratios and pressures [23].

MIE is increased by low temperature, low pressure, flow velocity, and moisture dilution [1,9,23,26–28]. Low temperatures increase MIE by increasing the energy required to heat the mixture to the ignition temperature [1,9]. Pressure can impact ignition performance by altering chemical kinetic behavior [9]. Ballal and Lefebvre [28] found that MIE is proportional to P^{-n}, where n depends on the equivalence ratio and flow velocity, as shown for Propane-air mixtures in Figure 2. Ono et al. [29] determined experimentally that the MIE of hydrogen-air mixtures are unaffected by relative humidity ranging from 0-90% at room temperature. However, in a recent numerical study Zhang, Gou, and Chen [27] found that MIE of methane-air-water mixtures increases with increasing water vapor dilution.

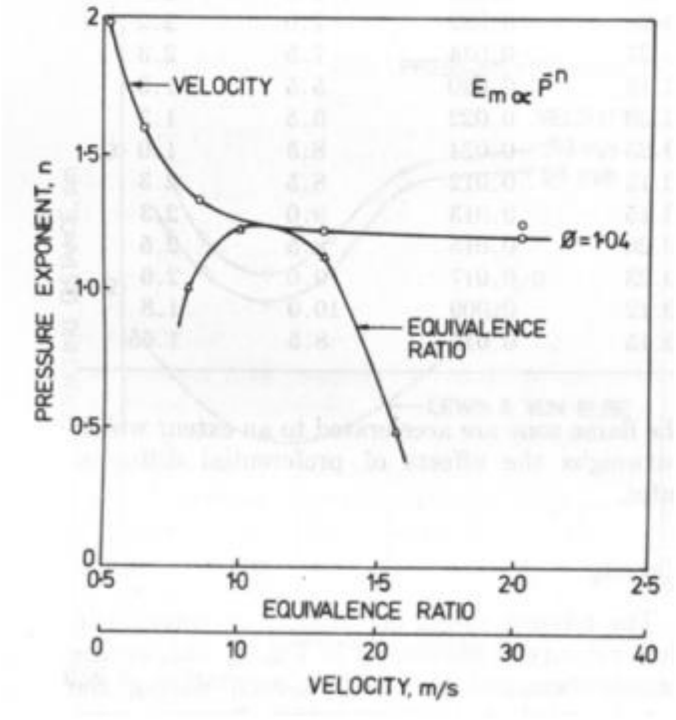

Figure 2 Pressure exponent n for adjusting the MIE of propane-air mixtures [28].

MIEs are fuel specific and allow for ready comparisons between different fuels for which MIE data is available. MIE has been well characterized for many fuels including Jet-A, Kerosene, Methane, Propane, and many others [23,25,30,31]. However, caution should be exercised when employing MIE trends to predict ignition for conditions that are different than those for which the MIE data was generated. Practical aviation fuels such as Jet-A are complex mixtures of many constituents, and a such can have significant variability in fuel chemistry. Significant discrepancies have been found in MIE values by different researchers at similar conditions [21,25,30].

2.1.2 Spark Kernels

Characterization of spark kernels is another method for investigating ignition. A spark kernel is a volume of gas that is heated by the spark produced by an ignition system [1,9]. Spark kernels can be investigated in reacting or nonreacting conditions. Reacting spark kernels are produced in the presence of ignitable mixtures of fuel and oxidizer. Investigation of reacting spark kernels can provide valuable insights into the ignition behavior of particular fuel-oxidizer mixtures [3,4]. However, reacting spark kernels are influenced by the fuel-oxidizer mixture and the characteristics of the ignition system. This makes it difficult to apply conclusions drawn from observations of reacting spark kernels to other fuels and ignition systems.

Non-reacting spark kernels are produced in environments that are not capable of ignition, such as air or inert gas. The behavior of non-reacting spark kernels is inherently dissimilar to ignition behavior in practical applications. However, observations of non-reacting spark kernels can provide valuable insights into the underlying mechanisms that contribute to ignition. Conclusions drawn from observations of non-reacting spark kernels are independent of fuel and can be used to evaluate a particular type of ignition system for a variety of different fuels. For this reason, the focus of this work is on nonreacting spark kernels.

Spark kernels are typically characterized by their spatial or thermal evolution. Spatial characterization focuses on fluid mechanic evolution and trajectory. Spatial evolution of spark kernels is important because combustion, and therefore ignition, are impacted by turbulence and mixing of fuel and oxidizer within the flame zone [1,9]. In addition, the fuel-air mixture within GTEs is typically non-homogenous. Therefore the placement of spark kernels within the flow field is critical for successful ignition [32]. The spatial development of non-reacting spark kernels has been characterized using visualization techniques such as high speed schlieren [14,15,33]. These techniques provide 2D projected images of the kernel shape and size evolution, and can be used for validation of numerical simulations. Spatial evolution of spark kernels is influenced by interactions between the kernel and surrounding fluid. For example, it has been shown that kernels form a toroidal vortex as they expand and draw in surrounding gases [11–17,30,34]. A review of vortex mechanics as it relates to spark kernels can be found in the thesis of Okhovat [30].

Thermal characterization focuses on the temperature evolution of spark kernels. Successful ignition is dependent on achieving sufficient temperature to initiate and sustain combustion reactions [1,9]. It is plausible that the discrepancies in MIE values noted earlier could be due in part to the volumetric distribution of energy, and therefore temperatures, within the spark kernel. Spark kernel temperatures are impacted by the characteristics of the spark ignition system, as will be discussed in Section 2.2. Differences in the ignition systems, and therefore spark kernel temperatures, used for determining MIE values could explain part of the discrepancies [24].

The temperature evolution of nonreacting spark kernels is dependent on fluid interactions, heat transfer processes, and the characteristics of the spark discharge system. As kernels entrain surrounding gas, the kernel temperature typically decreases. Spark kernel temperature distributions have been calculated from schlieren imaged density gradients for kernels produced in nitrogen at atmospheric and elevated pressures [11–13]. Reinmann and Akram reported temperature values of 30,000 and 23,000 K, after 1 and 5 microseconds, respectively [11]. Topham et al.[33] reported that mean temperatures of kernels produced by a pulsed plasma igniter were 400 and 20 K above the ambient temperature after 0.2 and 7 milliseconds, respectively, with a stored energy of 4.8 J in the ignition system. They also reported average temperatures of 40 and 10 K above ambient after 2 and 9 ms 0.98 J was supplied to the igniter. Sforzo et al. [14,15] used a laser-schlieren technique in combination with flow calorimetry to determine isothermal spark kernel temperatures in air at stagnant and crossflow conditions at atmospheric pressure. Sforzo et al.[15] reported temperatures of about 4100 and 1500 K after 60 and 200 microseconds, for kernels in a crossflow with 0.25 J deposited to two opposed cylindrical electrodes. These and more temperature results for nonreacting spark kernels can be found in Table 1.

Blunck et al. [17] developed a novel infrared thermography technique for determining temperature distributions of spark kernels. Blunck et al. reported a decrease in average temperature of 30% after traveling 2 cm for kernels ejected from a pulsed plasma jet igniter in quiescent conditions. Okhovat et al. [16,30] applied the technique to spark kernels produced by a sunken fire type igniter in quiescent and crossflow conditions. Okhovat et al. reported maximum average temperatures of 950 and 1250 K in quiescent and crossflow conditions respectively, with higher temperatures on the upstream side of the kernels ejected into crossflow. Both of these studies focused on temperatures of spark kernels at ambient pressure conditions. To the author's knowledge, there have been no attempts to determine spark kernel temperatures at subatmospheric pressures.

Table 1 Nonreacting spark kernel temperature results from literature.

Authors / Technique	Conditions	Ignition System	Temperature Results
Reinmann and Akram [11] / Interferogram	Gas: Nitrogen Flow: Quiescent Pressure: 1, 4 bar Time: 1; 5 µs	Electrodes: Opposed Pins, 2 mm gap Exciter Type: Capacitive Discharge Energy: 22-34 mJ	1 bar, 1 µs, 22 mJ: 30,000 K 4 bar, 1 µs, 34 mJ: 19,000 K
Topham et al [33] / Interferogram	Gas: Nitrogen Flow: Quiescent Pressure: Atmospheric Time: 0.4-20 ms	Electrodes: Opposed Pins Exciter Type: Stored Energy: 0.98, 4.8 J	0.98 J, 2 ms: 340 K 0.98 J, 4 ms: 314 K 4.8 J, 0.4 ms: 700 K 4.8 J, 5 ms: 330 K
Borghese et al. [13] / Interferogram	Gas: Nitrogen Flow: Quiescent Pressure: Atmospheric Time: 40-180 µs	Electrodes: Opposed Pins, 2 mm gap Exciter Type: Capacitive Discharge Energy: 14 mJ Current Duration: 50 ns	Peak at 40 µs: 1000 K Peak at 180 µs: 600 K
Sforzo et al [14] / Schlieren	Gas: Air Flow: Crossflow Pressure: Atmospheric Time: 0.06, 0.3 ms	Electrodes: Opposed Pins, 0.8-1.2 mm gap Exciter Type: Capacitive Discharge Energy:	0.06 ms: 12,000 K 0.3 ms: 1800 K
Sforzo et al [15] / LES Model	Gas: Air Flow: Crossflow Pressure: Atmospheric Time: 0.1-0.2 ms	Electrodes: Opposed Pins, 0.8, 1.2 mm gap Exciter Type: Capacitive Discharge Energy: 0.25 J	Peak: 2500-2800 K Average: 1300-2400 K
Kono et al. [12] / Analytical Model	Gas: Air Flow: Quiescent Pressure: Atmospheric Time: Various	Electrodes: Opposed Pins, 1.6 mm gap, 0.2 mm diameter Exciter Type: Discharge Energy: 9.1 mJ	Calc Peak, 0.05 ms: 1000 K Calc Peak, 0.2 ms: 460 K
Blunck et al [17] / IR thermography	Gas: Air Flow: Quiescent Pressure: Atmospheric Time: Various	Electrodes: Pulsed Plasma Jet Igniter Exciter Type: Capacitive Discharge Energy:	Proprietary
Okhovat et al [30] / IR thermography	Gas: Nitrogen Flow: Quiescent, crossflow Pressure: Atmospheric Time: 0.6-3.3 ms	Electrodes: Sunken Fire Igniter Exciter Type: Capacitive Discharge Energy:	Quiescent: 950 K Crossflow: 1250 K

2.2 Spark Discharge Fundamentals

Spark discharges are complex phenomena which can have widely varying characteristics and are dependent on many different factors. This section provides an overview of spark ignition systems, the process by which sparks are produced and transfer energy to the surrounding gas, and the impacts of spark characteristics on ignition performance.

2.2.1 Spark Ignition Systems

All spark ignition systems include a positive electrode, called the cathode, and a negative electrode, called the anode. The cathode and anode are separated by a small gap called the spark gap. In practical applications, these electrodes are typically insulated from each other and housed in a spark plug or igniter. The electrodes are excited by a power source that can be primarily capacitive, inductive, or both. Capacitive spark systems are generally capable of higher energy sparks [18]. Automotive ignition systems typically use inductive ignition systems due to cost [18], while aviation GTEs frequently use capacitive ignition systems due to the large amounts of energy required for ignition [35]. Igniters for aviation GTEs typically have an annular spark gap with the cathode in the center and the anode forming a ring around the cathode [35]. In experimental ignition systems the cathode and anode are frequently equally sized coaxially opposed pins separated by the spark gap [12,14,15,21,25,29,36]. Due to the highly transient nature of spark ignition, most components in the system including the wiring have some non-negligible capacitance, inductance, and resistance [18]. This means that the behavior of an ignition system is sensitive to the particular components from which it is made.

2.2.2 Spark Discharge Process

Spark ignition performance is heavily dependent on the characteristics of the spark discharge [37]. For this reason, a brief background on spark discharges is provided. Spark discharges include four phases: prebreakdown, breakdown, arc, and glow phases [18]. Typical voltage, current, and energy deposition traces for an experimental high energy capacitive spark discharge are shown in Figure 3.

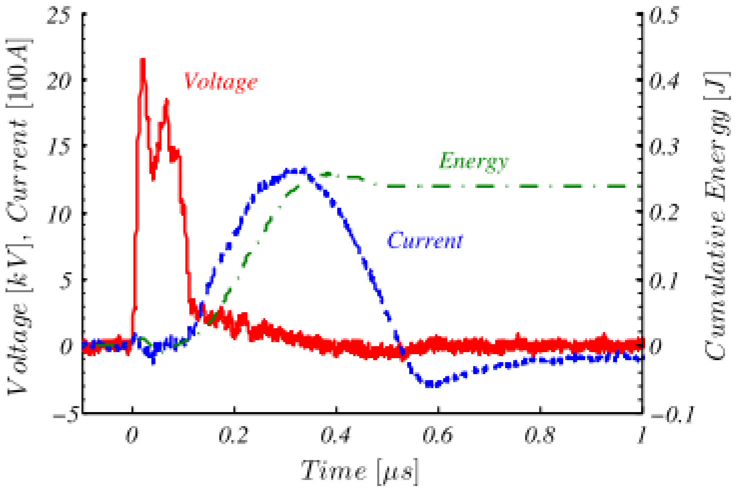

Figure 3 Representative voltage, current, and cumulative energy time traces for an experimental high energy capacitive spark ignition system [14].

The prebreakdown phase is the first phase of a spark discharge. Prebreakdown occurs when a strong electric field is applied across an open gas gap (i.e. an applied voltage difference between the anode and cathode). The electric field accelerates free electrons within the gas in the gap, causing them to collide with gas molecules. If the electric field is strong enough, these collisions can cause gas molecules to become ionized (i.e. lose an electron), thereby increasing the number of free electrons. As the number of free electrons increases, so do the number of collisions and a cascade effect known as electron avalanche is initiated. Electron avalanche is part of the Townsend Theory of breakdown [38–40]. As the level of gas ionization increases, the resistance of the gap decreases. When the resistance of the spark gap decreases below a critical level, current begins to flow across the gap marking the end of the beginning of the breakdown phase [18]. The prebreakdown phase duration is dependent on the voltage history applied to the gap, but is typically on the order of 1 ns. Faster voltage rise time and higher overvoltage above the breakdown voltage both cause prebreakdown to complete faster [18]. The breakdown voltage is dependent on the type of gas and the pressure and spark gap [38–40] as shown in Figure 4.

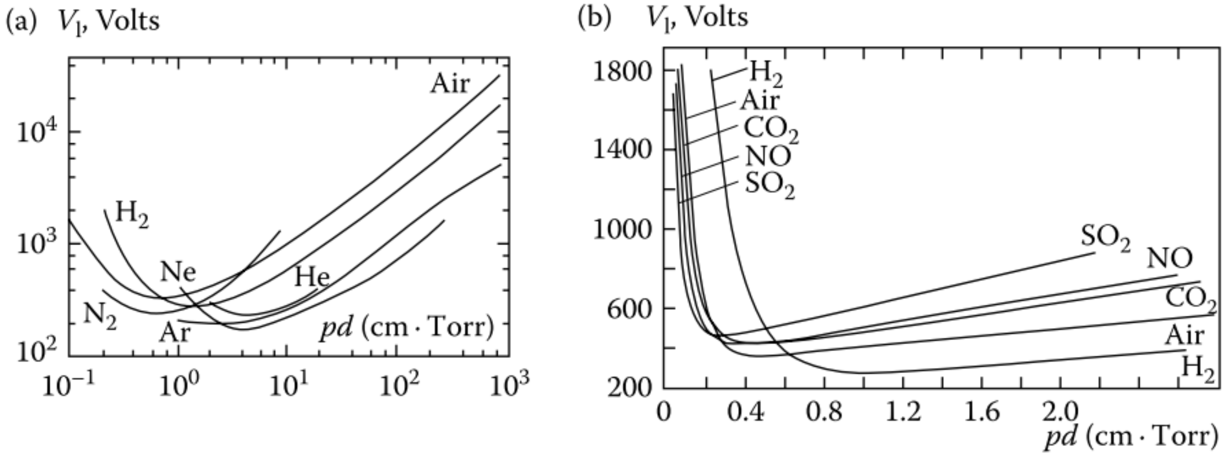

Figure 4 Relationship between breakdown voltage and the product of pressure and spark gap for various gases. (a) Higher pressure range and (b) lower pressure range [38].

During the breakdown phase, the resistance of the gap further decreases and current through the gap increases rapidly. Because the resistance decreases, the voltage across the gap also decreases. Voltage can drop from tens of kV to hundreds of volts within 20-50 ns [18]. Breakdown is characterized by efficient conversion of electrical energy into plasma, which rapidly expands [18]. This rapid expansion is driven by rapidly rising pressure which is in turn driven by the rapid increase in temperature due to the generation of plasma. The pressure rise is so fast that it produces a shock wave which travels outward at supersonic speed [18,41]. Some argue that while the plasma is extremely hot, little energy is lost to radiation due to the very short wavelengths emitted [18]. Others claim that radiation from the initial shock wave can dissipate as much as 50% of the electrical energy deposited [37]. A low-pressure zone follows the shockwave and draws in cold surrounding gas, enhancing mixing and reducing convective heat losses to the electrodes [12,18,41]. Plasma temperature can be on the order of 60,000 K, and is completely dissociated and almost completely ionized. As a result, the plasma in the spark volume is at its maximum thermal energy capacity; greater energy inputs create larger volumes of plasma rather than higher temperatures [18].

The arc phase follows breakdown and is characterized by a high current flowing through low resistance plasma connecting the electrodes. In high energy capacitive ignition systems this current can be on the order of 1 kA [14,15,20]. To support the current through the gap, additional electrons are required and are supplied by small molten pools of metal on the electrodes. The arc phase has a longer duration than the previous two phases, and can last from 1 to hundreds of μs [37]. As a result, there is more time for heat loss to the electrodes [18,37]. Conversion of electrical to thermal energy (to the gas) is about 50% efficient in the arc phase [18].

The glow phase is the final phase of the spark discharge. The remaining energy stored in the ignition circuit is transferred to the spark gap. As the stored energy is depleted, the power decreases leading to a decreasing current and increasing resistance across the spark gap. Because the resistance increases, the voltage may increase slightly during this phase. The energy in a glow discharge is deposited into a small volume approximating a point near the cathode. As a result of the proximity to the cathode, there is a large thermal loss due to conduction to the cathode. Energy conversion efficiency is about 30% during the glow phase [18]. The glow phase can last the longest, with durations in the ms range.

2.2.3 Impacts of Spark Discharge Characteristics on Ignition

Only a small fraction of the electrical energy released in a spark discharge contributes to ignition. The remaining energy is dissipated through various forms of heat loss. In a flowing mixture, heat loss from the spark kernel is dominated by forced convection and radiation losses from the initial shock wave; conduction, turbulent diffusion, and thermal radiation are all negligible. These losses are increased by increases in both velocity or pressure [28,37].

Point sources have been shown to be more effective than line sources, so it may seem that the glow discharge would be more favorable than an arc discharge. However, due to the close proximity of a glow discharge to the cathode, the heat loss to the cathode counteracts the advantages of being a point source. As a result, arc discharges are preferred for ignition. Controlling the voltage supplied to the gap such that it occurs in 'rectangular' pulses with respect to time can be used to control the length of the arc phase and minimize the glow phase. Increasing the arc phase duration decreases the ratio of energy lost in the initial shock wave relative to the total energy deposited in the spark [37].

Ono et al. [29] found that spark durations ranging from 5 ns to 1 ms had no effect on the MIE of hydrogen-air mixtures. However, Ballal and Lefebvre [37] found that a spark duration of 60 μs is optimal for flowing stoichiometric propane-air. Ballal and Lefebvre [28] also found that turbulence intensity had no effect on the optimum spark duration because the spark timescale is much smaller than the shortest turbulence time scale.

Chapter 3 Experimental Approach

This chapter provides a description of the experimental approach for determining temperatures of spark kernels produced at sub-atmospheric pressures. Details regarding the test facility, data collection, analysis methods, and technique validation are presented.

3.1 Experimental Arrangement

The experimental arrangement is shown in Figure 5. Spark kernels were generated using a sunken fire type igniter (Champion Aerospace CH31627), pictured in Figure 6, with outer diameter of 12 mm, and an annular spark gap of 1.5 mm. The igniter was powered by a high voltage exciter (Champion Aerospace CH305050), which was measured to reach a maximum potential of 7 kV when the igniter was disconnected. The sparking frequency was approximately 2.6 Hz. The igniter was connected to the exciter using 10-gauge 15 kV rated wire (McMaster-Carr 8296K29) of minimum length (about 0.5 m). The igniter was located inside a vacuum chamber as shown in Figure 5.

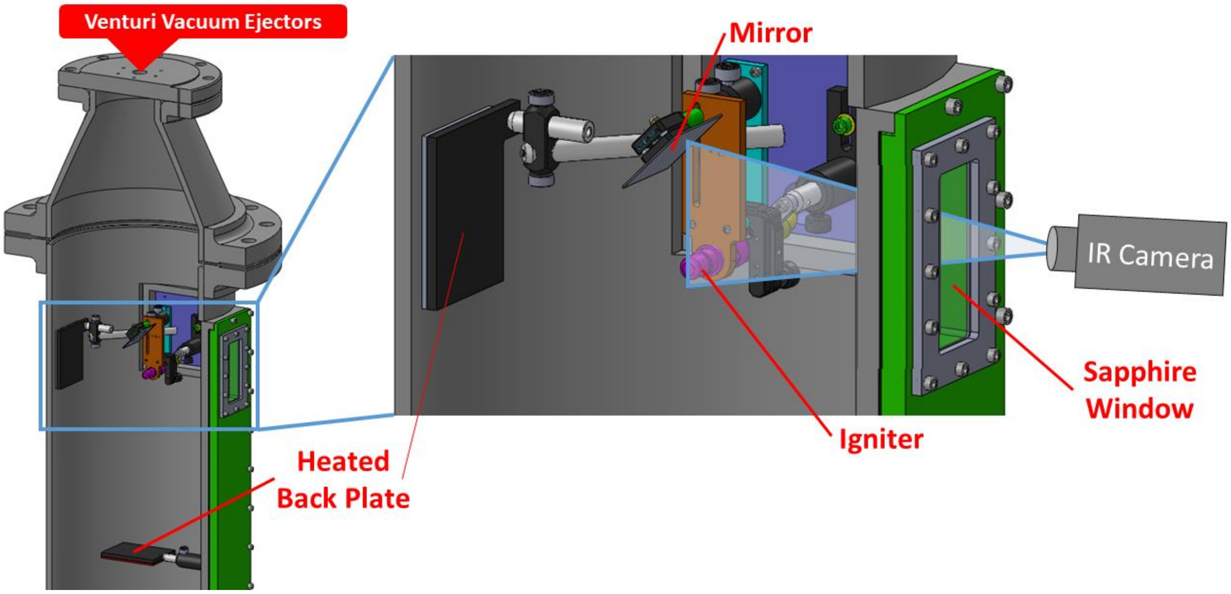

Figure 5 Experimental arrangement for measuring the temperatures of spark kernels at sub-atmospheric pressures.

Figure 6 Photograph of the igniter used in this work.

A mid-wavelength (1-5µm) infrared camera with a cryogenically cooled InSb detector (FLIR SC6700) was used to measure radiation intensity emitted from kernels. Integration time was set to 82 µs, similarly to that used by Okhovat [30]. The camera reports photon counts rather than radiation intensity. The camera was calibrated using a blackbody emitter (Electro Optical Industries CS1250-100). The camera was calibrated at eight evenly spaced temperatures from 50 to 225 °C which spanned 10 to 90% of the detector's dynamic range (i.e. 14 bits or 16,383 photon counts at saturation). A calibration curve was created to convert photon counts reported by the camera to radiation intensity, and was linear with an R^2 value of 0.998. A frame rate of 1500 Hz was selected to balance between fast data capture and temporal resolution. The maximum image resolution at the selected frame rate was 120x64 pixels. The lens had a fixed 50mm focal length, so the image resolution dictated that the camera be located 2.2 meters from the igniter in order to view the entire area of interrogation.

An aluminum mirror (ThorLabs ME2S-G01) was used to provide a side view of the kernel within the field of view of the camera. The side view was used for determining the path length through the kernel along the camera's line-of-sight. The gases present in air, namely H_2O and CO_2, emit radiation in bands centered at 2.7 and 4.3 µm, respectively, within the camera's detection limits (i.e. 1-5 µm). The aluminum mirror was selected because it had reflectivity in excess of 95% for the spectra of interest. The camera viewed the kernel and mirror through a sapphire window. Sapphire was selected because it had a transmissivity in excess of 85% for the spectra of interest. The window dimensions were 50x110x1.2 mm, which were optimized to balance the viewing area, transmission losses due to window thickness, and window strength to hold the vacuum pressure.

The camera was spatially calibrated using a machinist's scale, as shown in Figure 7. The resolution was found to be 0.64 mm/pixel, with square pixels. A bare metal stainless steel machinist scale with painted gradations was used for the spatial calibration. Stainless steel typically has an emissivity less than 0.1, while many paints (regardless of color) have emissivities greater than 0.9; this difference in emissivity provided good contrast for viewing the gradations on the scale in the infrared. The scale was also heated to increase the radiation emitted by the painted gradations, further enhancing the contrast. A layout snapshot was collected at the beginning of testing using a longer integration time (to allow the edges of the window, mirror, and igniter to be visible) as shown in Figure 7. This layout snapshot was displayed in MATLAB®, and the edges of the window, mirror, and igniter were manually selected. These edge selections were used to define the front and side views, as well as regions of interest (ROIs) used for some image processing steps. The cyan outlined region in the lower half of the image is the front view, and the magenta outlined region at the top is the side view provided by the mirror.

Radiation emissions from the kernels alone were not sufficient for the camera to detect within its linear response range, therefore heated plates were used to increase the radiation received by the camera. Background subtraction was performed to isolate radiation emitted by the kernels, as described in Section 3.3.2. The plates were placed behind the area where kernels were generated, such that the camera viewed a plate as the background for both the front view and the side view provided by the mirror. The plates were coated with flat black paint, which provided a uniform emissivity. A heat blanket was bonded to the back of each plate, which were made from aluminum to promote thermal uniformity. A thermocouple was embedded in the aluminum substrate, and the temperature of each plate was controlled using PID controllers. The temperature of the plates was 100°C, such that camera detected approximately 3000 photon counts from background radiation.

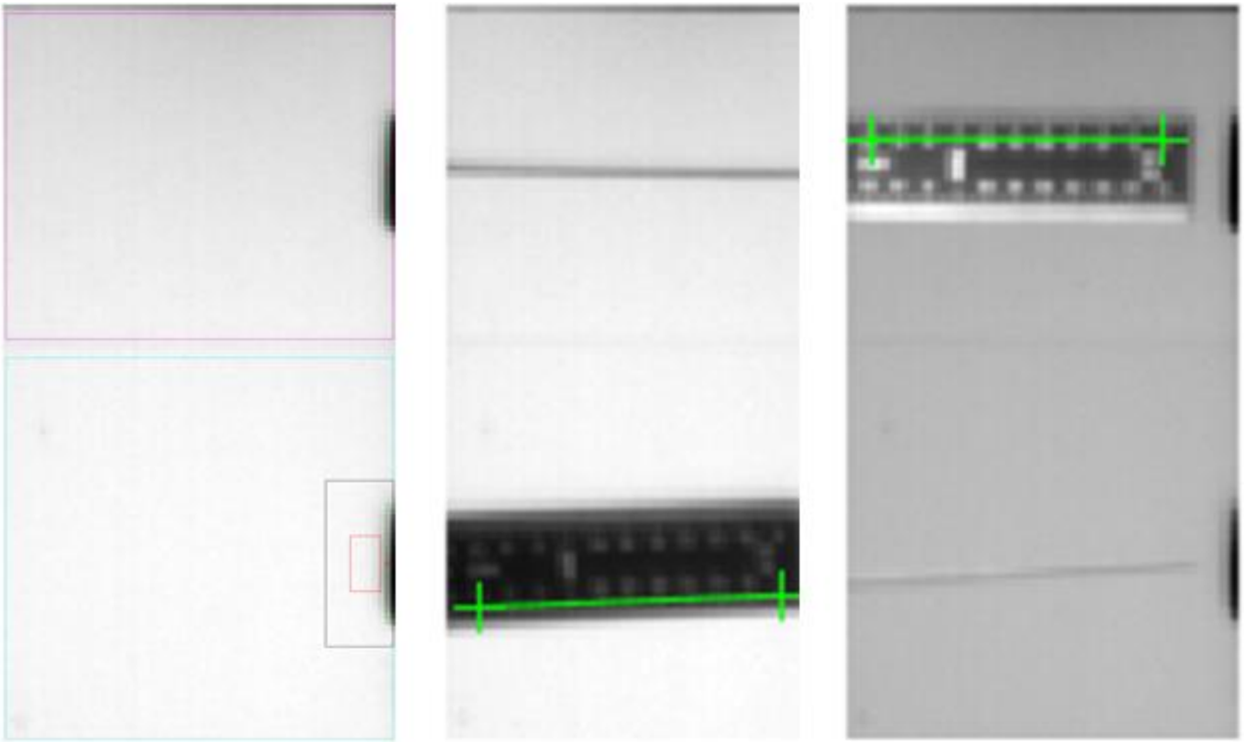

Figure 7 Layout of the area of interrogation as viewed by the IR camera (Left), and spatial calibration images for the front view (center) and side view (right). In the layout image, the large regions outlined in cyan and magenta are the front and side views, respectively. The red rectangle represents the ROI used for identifying plasma, and the black rectangle represents the region that was masked from analysis (these ROIs are discussed in Section 3.3).

A jig was used to align the igniter, mirror, and camera. The igniter and mirror were mounted to the jig, with the mirror attached via a kinematic mount for angle adjustment. The jig was placed on an optical table and a laser square emitting two perpendicular laser points was used to align the igniter, mirror, and camera. Once the jig and camera were aligned using the optical table, a hole-sight was installed and calibrated. The hole-sight was used to align the camera and the jig when installed the vacuum chamber. Once aligned, the hole-sight was removed so as not to interfere with the camera’s view of the kernels. The hole-sight was located to the jig using dowel pins, allowing it to be removed and reinstalled without requiring recalibration.

The vacuum chamber was evacuated using two venturi ejectors (VACCON JS-350) operating continuously in parallel. The absolute pressure in the chamber was measured using a precision pressure transducer (OMEGA Engineering PCL-1B). The chamber pressure was adjusted by controlling the supply pressure to the ejectors. Supply pressure to the ejectors was manually adjusted until the pressure in the chamber stabilized at the desired value. Spark kernels were investigated at pressures ranging from 300 to 1000 mbar.

The concentrations of H_2O and CO_2 in the room air were measured using an environment monitoring sensor (Sensirion SCD30). The sensor had an automatic self-calibration algorithm which adjusted a linear offset so that the lowest reading in the last 30 days corresponded to 400 ppm CO_2. This calibration method, while convenient for monitoring CO_2 levels for safety purposes, was deemed inadequate for scientific use. Furthermore, the air in the laboratory had been previously found to have CO_2 concentrations in the 600-ppm range using a calibrated high accuracy gas analyzer (Campbell Scientific IRGASON). Therefore, the SCD30 sensor was calibrated using a reference gas mixture of nitrogen and 600 ppm CO_2, mixed using thermal mass flow controllers. The nitrogen was controlled using a calibrated high flow rate controller. The flow controller for the CO_2 was older and out of calibration, so a positive displacement flowrate calibrator (Sensidyne Gilibrator-2) was used to determine the correct setting to accurately achieve the target CO_2 concentration.

3.2 Inverse Deconvolution Technique

The infrared camera measures photon counts, not temperature or even radiation intensity. A blackbody calibration allows the photon counts to be converted to radiation intensity as described above. Temperature can then be calculated from the radiation intensity, based on knowledge about the source of the substance that is being measured. For a solid or liquid surface, only the emissivity must be known (assuming there is no reflected radiation from other sources). Determining temperature for a gas is more complex. Unlike solids and liquids, which emit radiation only from the surface, the radiation emitted by a gas is affected by the line-of-sight thickness of the emitting gas. Gases also emit and absorb radiation in discrete wavelength bands. Therefore, determination of gas temperature based on measurements of infrared radiation intensity requires knowledge of both the line-of-sight thickness of the gas and empirical data about the emission and absorption behavior of the gases being measured.

An inverse deconvolution technique developed by Blunck et al [17] was used to convert the spark kernel radiation intensity measurements collected by the camera to temperature. First, the radiation transfer equation (1) for a non-scattering participating medium,

$$I_\lambda = I_\lambda(0)\exp(-\tau_\lambda) + \int_0^{\tau_\lambda} I_{b,\lambda}(\tau_\lambda^*)\exp(-\tau_\lambda + \tau_\lambda^*)\, d\tau_\lambda^*,$$

$$\text{where } \tau_\lambda^* = \int_0^s \kappa_\lambda\, ds, \qquad (1)$$

was solved to get the spectral intensity (i.e. IR spectrum) emitted from the kernels. Equation (1) was solved using a narrowband radiation model (RADCAL) [42]. RADCAL calculates spectral radiation emissions based on built-in empirical emission and absorption data for select gases, and user inputs of temperature, path length, gas composition, pressure, and background wall temperature. The background wall temperature was set to 0 K since radiation from the background was eliminated, as described in Section 3.3.2. The spectral intensity calculated using RADCAL was convolved with the known spectral transmission profiles for the window and lens, and the spectral response profile for the camera detector, to account for losses through these components. Once convolved, the spectral intensity was integrated over the camera detector's sensitivity range so that the calculated integrated intensity could be compared to the intensity measured by the camera. The technique can be represented by equation (2):

$$I_{measured} = I_{calculated} = \int_{\lambda_1}^{\lambda_2} \prod_i (I_\lambda \alpha_i)\, d\lambda \tag{2}$$

$$\text{where } I_\lambda = RADCAL(T, s, c),$$

where λ_1 and λ_2 are the respective lower and upper limits of the camera detector sensitivity range, α_i are the response profiles for the window, lens, and detector, s is the line-of-sight path length, c is the gas composition of the kernel, and T is the guessed and iterated temperature of the gas. An illustration of the inverse deconvolution technique is shown in Figure 8.

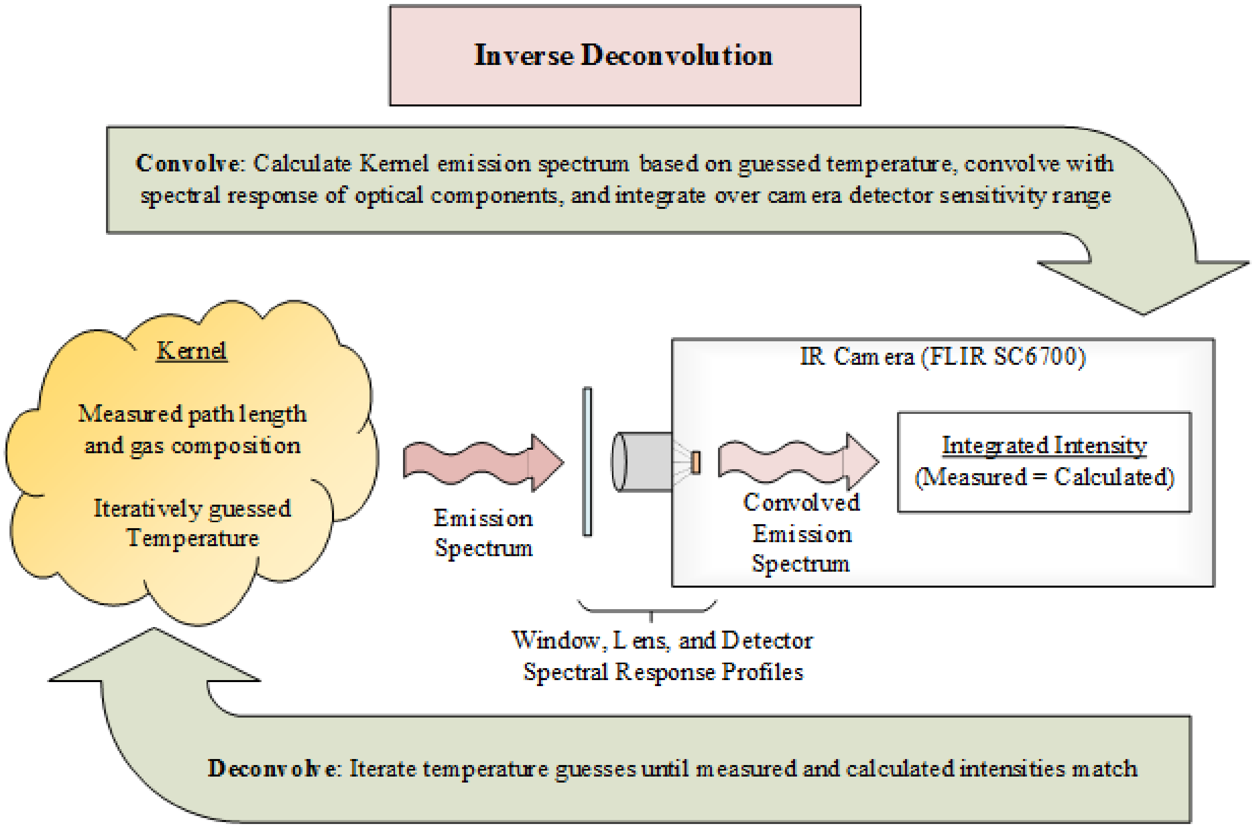

Figure 8 Graphical summary of the inverse deconvolution technique used in this work.

The technique as described must be applied to each pixel of each image, and requires a cumbersome amount of computational resources. This is exacerbated by the iterative nature of the process, since RADCAL must be executed multiple times before converging. Since many kernels have pixels that are very similar in temperature, repeating this process for each individual pixel is an inefficient use of computational resources. Okhovat et al [16] found that using RADCAL and the convolution and integration steps to pre-calculate a database of possible intensity values was faster than the iterative method when processing large numbers of images. A database was pre-calculated for a range of possible path lengths and temperatures for each test day. The databases were day-specific based on the average measured concentrations of H_2O and CO_2 in the air in the room each test day. Temperatures were interpolated from these precalculated databases as a function of measured intensity and path length. An example of such a database is represented by the three-dimensional surface shown in Figure 9.

The databases were created with temperatures ranging from 300 to 5000 K in 100 K increments, and depths ranging from 0.5 to 40 mm, with increments of 0.5 mm. Any pixel with an intensity or depth that was outside these ranges was not processed. The lower temperature limit of 300 K was selected because this was approximately equal to the ambient room temperature, and it was not possible for temperatures below ambient to exist. No kernels had values above 5000 K, so this value was selected as the maximum for the database. The lower depth limit of 0.5 mm was selected because this is smaller than the spatial resolution for each pixel. The upper limit of 40 mm was selected because there were no kernels with greater depths.

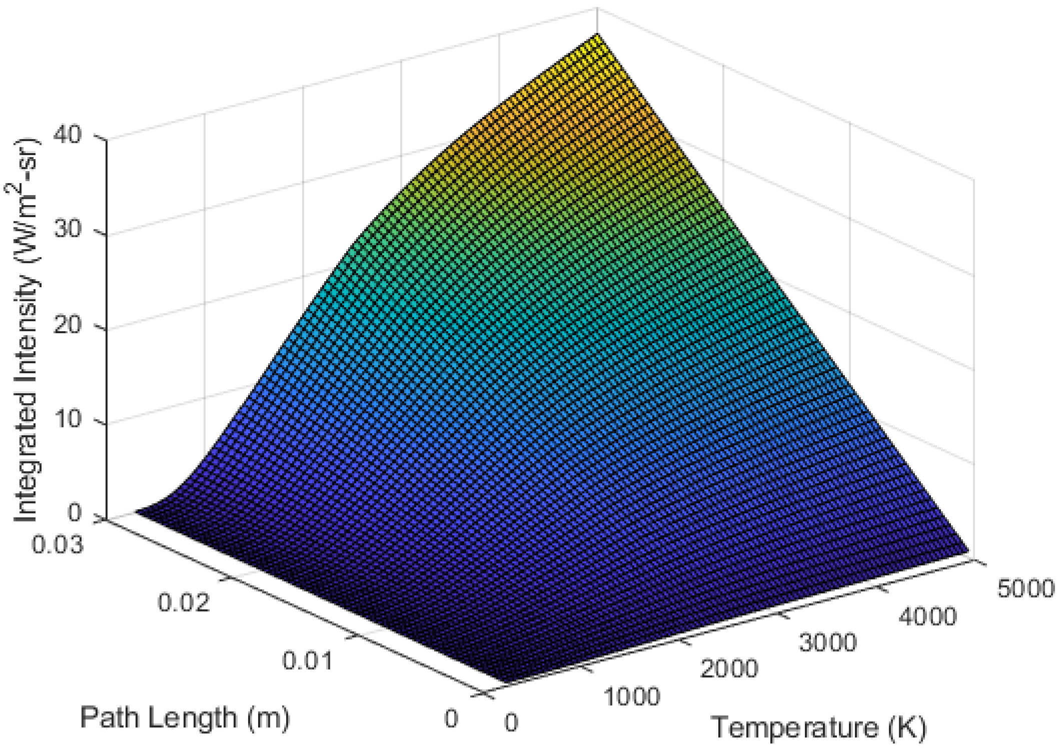

Figure 9 Graphical representation of a temperature lookup database.

The databases were also dependent on the pressure within the vacuum chamber. However, it was found that the intensity was linearly proportional to pressure for nearly all values. Therefore, to reduce the computational resources required to generate the databases, RADCAL was used to generate a single database at 1 atm. Additional databases were then created from the 1 atm database by multiplying the calculated intensity magnitude by the pressure ratio relative to 1 atm. This simplification was evaluated by comparison with intensity values calculated using relevant pressures as an input to RADCAL. The intensity was found to agree within less than 0.5% for most temperatures and path lengths, and within 2% for the worst case of longest path length, lowest temperature, and lowest pressure.

3.3 Image Processing

With the database created, the images were processed to determine temperatures. Image processing included finding kernel events in the datasets, converting them from photon counts to intensity, eliminating background radiation to isolate the radiation from the kernels, finding the edges of the kernels, determining the line-of-sight path lengths, and interpolating the temperatures from the database. Once temperatures were determined, phase-averaged temperature images and spatial temperature maps were generated, and metrics such as average temperature, volume, and sensible energy were calculated. Details of the image processing are discussed in the following subsections.

3.3.1 Identifying Kernels in the Data

The igniter sparking frequency was not synchronized with the camera, so the datasets were scanned to find kernel events. Each data set included multiple kernel events, with several consecutive frames for each event. However, only kernel events for which plasma was visible in the first frame were considered for analysis. The time after the spark was required to be known for each image. However, if plasma was not visible in the first frame of an event the spark discharge could have occurred anytime within the 0.67 ms between the first frame and the preceding frame. If plasma was visible in the first frame of an event, it was assumed that the spark discharge occurred sometime during the exposure (82 μs). Events for which the first frame has visible plasma were considered for analysis. The beginning frame (frame zero, containing plasma) of each event was considered to be zero seconds, and each subsequent frame (i.e. frame 1,2,3, etc.…) in the event was 0.67 ms later.

A frame was assumed to contain plasma if the average photon count in an ROI identified in the layout was above a set threshold. Plasma is much hotter than the heated gas in the kernels, and as a result emits much more radiation. Due to the increased radiation from the plasma, it could be expected that the image would be saturated (i.e. exceed the maximum number of photons the detector can count) in the region of the plasma. It would follow that plasma could be identified by a wholly saturated ROI in the region where plasma is expected to occur. However, not all images that were manually considered to contain plasma had a saturated region. The camera has a 14-bit dynamic range, which implies a theoretical saturation at 16,383 photons. In practice the saturation limit for the camera was inconsistent. During blackbody calibration, it was found that the photon count for each pixel could reach different maximum values below the theoretical maximum. In addition, the spark does not always occur in the same location due to the annular geometry of the electrodes. Because the spark location was inconsistent, the ROI for plasma detection had to be large enough to capture all locations where the plasma could occur, which meant that it also included regions where there was no emission from plasma.

An ROI approximately the width of the igniter was used to distinguish between frames with and without plasma. A random set of 500 kernel events at varying pressures was manually sorted into two groups depending on whether the first frame did or did not contain plasma. An ROI was defined and averaged for both groups, as shown in Figure 10. Different ROI sizes and locations were analyzed. The ROI shown in Figure 10 was selected because it was the most effective at distinguishing between images that did contain plasma and images that did not. A minimum threshold of 14,000 photons on average in the ROI was found to be acceptable for identifying plasma in the image, as shown in Figure 10.

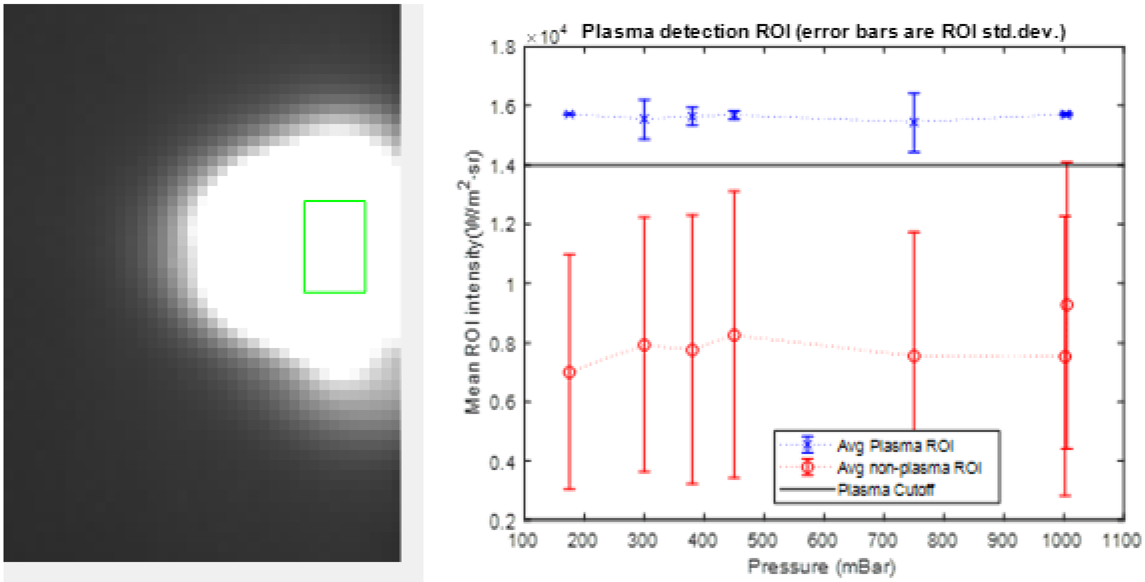

Figure 10 Plasma identification ROI and comparison between plasma and non-plasma first event frames. Error bars represent 1 standard deviation from the mean for each datapoint.

Kernels were detected up to 4 ms after plasma was detected. Some kernels were detected after 4 ms, but had average apparent sizes so small that they were represented by less than nine pixels. Therefore, data is only reported up to 4 ms after plasma was detected.

3.3.2 Conversion to Radiation Intensity, and Background Subtraction

Once kernel events were identified, the photon counts collected by the camera were converted to radiation intensity using the calibration curve described in Section 3.1. Then, background subtraction was performed to isolate radiation from just the kernels. The background was taken to be the average of the five frames preceding frame zero (i.e. the frame containing plasma). These 5 background frames were averaged into a single image, and converted to radiation intensity. Then, the average background intensity was subtracted from each frame identified in the spark event. This background subtraction process yielded images containing only radiation emitted from the kernels.

3.3.3 Edge Detection and Path Length Measurement

Next, edge detection was used to locate the kernel within in each image. Okhovat [30] used a binarization with a constant threshold of 0.1 W/m2-sr to identify kernel edges. Any pixel that was above the binarization threshold was given a 1, and any pixel that was below the threshold was given a zero, creating a map of where the kernel was in the image. Several other methods of edge detection were considered as possible replacements for threshold binarization including the Canny, Sobel, Prewitt, Roberts, and LoG methods. However, threshold binarization was selected because this method directly distinguished between radiation from kernels and background radiation levels. Great care was taken when selecting the threshold for determining kernel edges, as the calculated temperature and energy are sensitive to this parameter, as discussed in Section 3.6. Rather than the constant threshold employed by Okhovat, this work used a day-specific threshold that was 4 standard deviations above the background noise level to ensure that the kernels were distinguished from the background radiation emission. The threshold magnitudes were similar despite the difference in their determination, with the threshold here ranging from 0.1 to 0.4 W/m2-sr.

The background noise level was determined by calculating the average and standard deviation of an ROI in a region where no kernels were detected. All of the data for a given test day was identified and background subtracted. Then, all images with kernels were overlaid, and an ROI was selected in a region where no kernels were visible. The average and standard deviation of this ROI spanning all considered images for that test day were calculated, and used to determine the binarization threshold.

The line-of-sight path length was determined from the front and side views as shown in Figure 11. The kernel was approximated as a stack of elliptical slices, and the width and depth axes of each elliptical slice was determined from the front and side views captured by the camera and mirror. The path length of any given pixel was calculated as the chord length through the corresponding ellipse slice in a direction parallel to the depth axis, as shown in Figure 12.

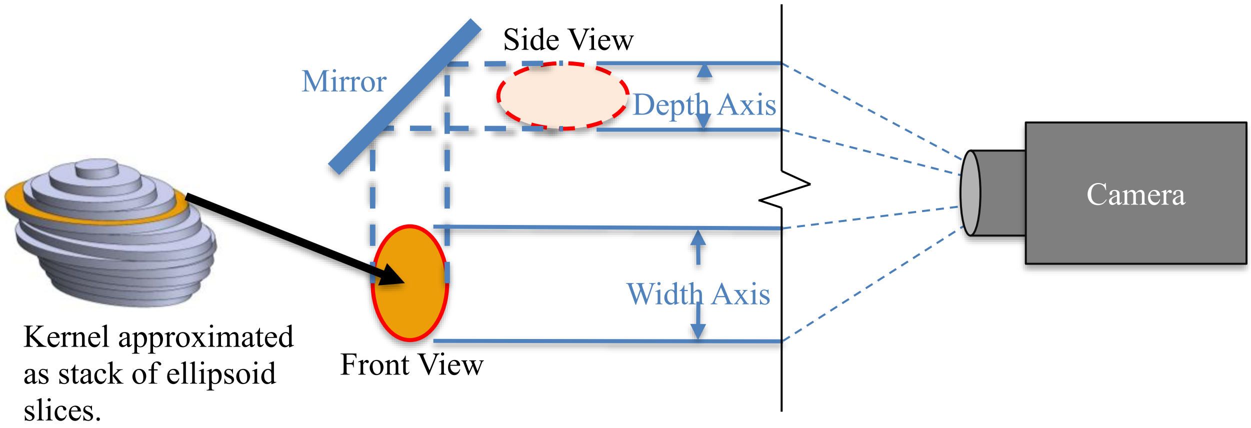

Figure 11 Illustration of determining the ellipse width and depth axes from the front and side views.

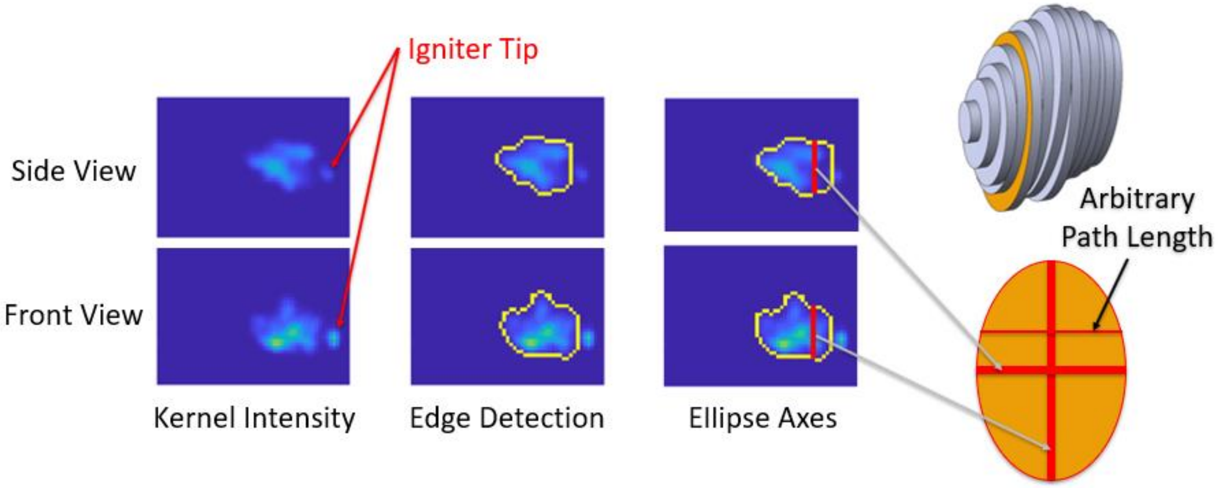

Figure 12 Example of ellipse axes determination from edge detection, and line-of-sight path length as the chord through an ellipse slice.

3.3.4 Temperature Determination

Once both the kernel radiation intensity was isolated and the path lengths determined, the temperature was interpolated using the database described in Section 3.2. A 2-dimensional interpolation look-up algorithm was implemented to interpolate the temperatures from the database. Since the temperatures in the database were not unique, great care was required to implement a stable and reliable interpolation algorithm. The implemented algorithm determined the temperature using a two-step process. First, a list of possible temperatures was identified corresponding to the specified path length. Second, the temperature corresponding to the specified intensity was interpolated from the list of temperatures. This interpolation method was evaluated by interpolating temperatures for all combinations of 30 random path lengths and intensities (900 temperatures total), with 100% of the interpolated points intersecting the surface represented in Figure 9.

3.3.5 Image Filtering

Once temperatures were determined for all collected data for a given day, filters were applied to mitigate biasing due to artifacts. There were two phenomena that were found to adversely affect the accuracy of calculated temperatures. The first was radiation from the igniter tip, which was heated from generating the spark. The igniter tip emitted relatively large amounts of radiation and caused some light bleed to neighboring pixels in the infrared camera, as shown in Figure 13. To mitigate this, a rectangular region in the vicinity of the igniter tip was masked from further analysis. This mask was 1.4D (i.e. 1.4 igniter diameters) wide, and extended 0.5D beyond the igniter tip. As an added benefit, this also masks what could have been misleading information about the kernels in the region adjacent to the igniter tip. Due to the limited frame rate of the camera, kernel generation and initial liftoff from the ignitor tip could not be interrogated. Results that would have been displayed in the region adjacent to the igniter would have been inaccurate and misleading.

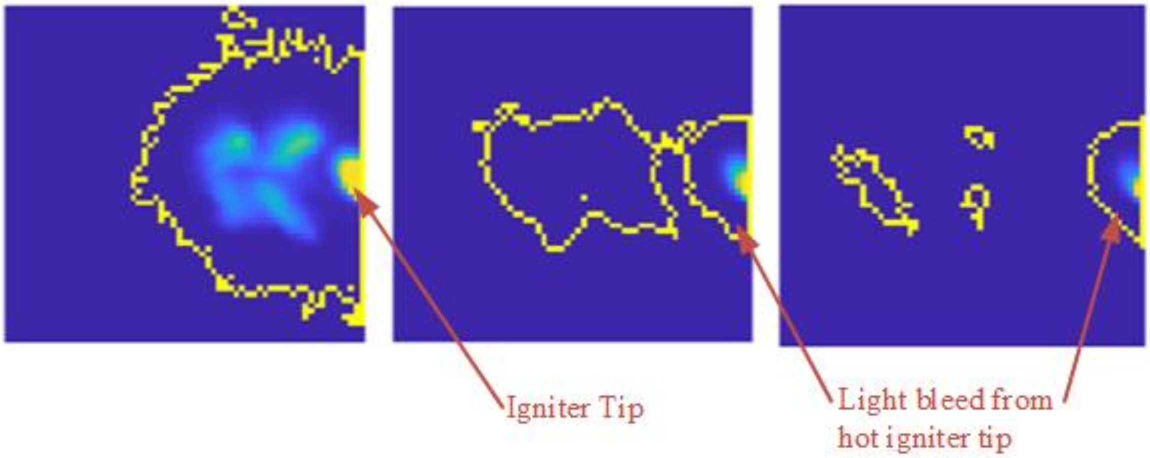

Figure 13 Excessive radiation emissions and light bleed from the heated igniter tip.

The second phenomenon that could bias the results was radiation emissions from material ablated from the igniter tip (i.e. embers generated during the spark event). The inverse deconvolution technique is only valid for determination of gas temperature, so temperatures determined based on radiation emissions from embers (presumed to be either solid or liquid) are invalid.

Ablated embers followed varying trajectories and frequently traveled within or very near to the kernels, so eliminating them by not considering data in a particular region was impractical, and the image resolution was insufficient to use existing automated image processing algorithms to robustly identify and eliminate radiation emissions from embers. Okhovat [30] encountered similar difficulties, and solved the problem by manually excluding spark events containing embers from analysis. Excluding events containing embers was possible for that work, because at atmospheric pressure the igniter ablated embers intermittently. However, the rate of ember ablation increased with decreasing pressure. At some of the pressures investigated in this work (i.e., 450 mbar and below) embers were observed in nearly all kernel events.

For this reason, analysis was performed to estimate the impact of the presence of embers on the temperatures determined in this work. A random subset of 249 atmospheric-pressure kernels was manually inspected, and events containing embers were eliminated. Of the 249 kernels inspected, 46 kernels had no visible signs of embers. The average temperature evolution of the group of kernels that did not contain embers was compared to the average temperature evolution of the entire set of 249 kernels. The impact of embers on the initial kernel results was minimal, but took on a greater role at later stages of the kernel development. Specifically, the average temperature for both groups differed by 0.4-1.4% at times from 0.67 to 2.67 ms after plasma, but differed by 3.1% after 3.33 ms and 8% after 4 ms. Based on this analysis, kernel temperature trends are believed to be reliable from 0.67 to 3.33 ms, but should be disregarded after 3.33 ms. It was decided that since the earlier stages are the most important for real world ignition applications, significant efforts at eliminating embers were not required.

Nonetheless, an attempt was made to minimize the impacts of ablated material on the reported temperatures. As noted above, kernel trajectories were reasonably consistent, while ember trajectories varied greatly. While this made elimination of embers traveling within, in front of, or behind the kernels challenging, embers whose trajectories diverged from the kernels were easily eliminated. Pixels that detected elevated radiation in less than 10% of the images containing kernels at the same pressure and time were eliminated from further analysis. This ember elimination filtering is illustrated in Figure 14.

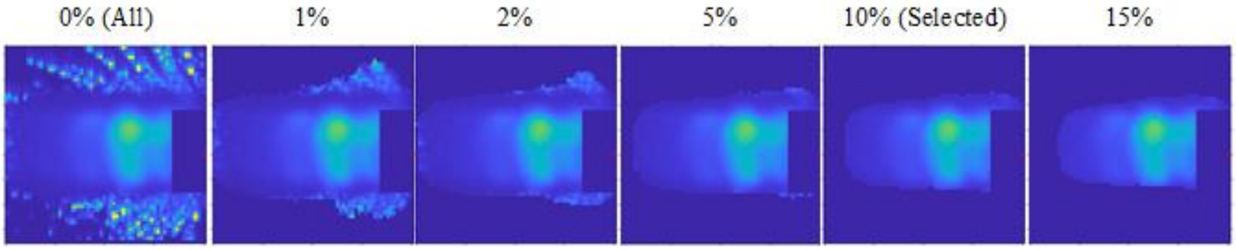

Figure 14 Example of ember elimination by ignoring pixels that infrequently detected elevated radiation emissions. These images show the average intensity of images containing kernels. The same average image is shown in each panel, with different thresholds for eliminating pixels based on radiation detection frequency. Thresholds ranging from 0% (i.e. no elimination) at the left to 15% at the right were evaluated. A threshold of 10% was selected.

3.3.6 Calculations for Average Temperature, Radiation Intensity, Kernel Volume, and Sensible Energy

The average temperature and intensity were determined based on the apparent volume of the kernels. The volume was calculated from the path-length-weighted average temperature and intensity for each kernel:

$$X_{avg,i} = \frac{\sum_k X_{i,k} s_{i,k}}{\sum_k s_{i,k}}, \tag{3}$$

where X represents either temperature or intensity, i represents each individual kernel image, and k represents each pixel within the kernel in the current image. This collapsed the temperature and intensity images for each kernel into scalar values that were then averaged and used to generate the trend plots reported in Chapter 4.

The volume of each kernel was determined from the path lengths and the spatial calibration of the camera:

$$V_i = \sum_k s_{i,k} a \tag{4}$$

where a is the area represented by each pixel.

The sensible energy for each kernel was determined relative to the ambient air temperature in the room. The sensible energy for each kernel was determined from:

$$E_{sensible,i} = \sum_k \rho_{i,k} V_{i,k} (h_{i,k} - h_\infty) \tag{5}$$

where the density, ρ, was evaluated at the line-of-sight path-averaged temperature for each pixel, $T_{i,k}$, the volume, $V_{i,k}$, was the line-of-sight path length, s, multiplied by the pixel area (similarly to the volume calculation above), and $h_{i,k}$is the enthalpy evaluated at the pixel temperature, and h_∞ is the enthalpy evaluated at the ambient air temperature.

3.4 Electrical Energy Measurement

The electrical energy delivered to the igniter was measured by collaborators at the Air Force Research Laboratory. Electrical energy deposition was measured for comparison with the calculated sensible energy determined using the inverse deconvolution technique. The electrical energy was calculated as

$$E_{elec} = \int_0^\infty V(t)i(t)\,dt \tag{6}$$

where *V* and *i* are respectively the voltage and current across the spark gap. In practice, the infinite upper bound of the integral is terminated when the current returns to zero (i.e. no further energy is deposited), which was on the order of 20 μs. Due to the large magnitude of current, the wires have non-negligible resistance and will dissipate energy, biasing the measurement. For this reason, the voltage was measured as close as possible to the igniter electrodes. Placement of the current monitor is less sensitive, as the current is effectively the same at all locations in the loop.

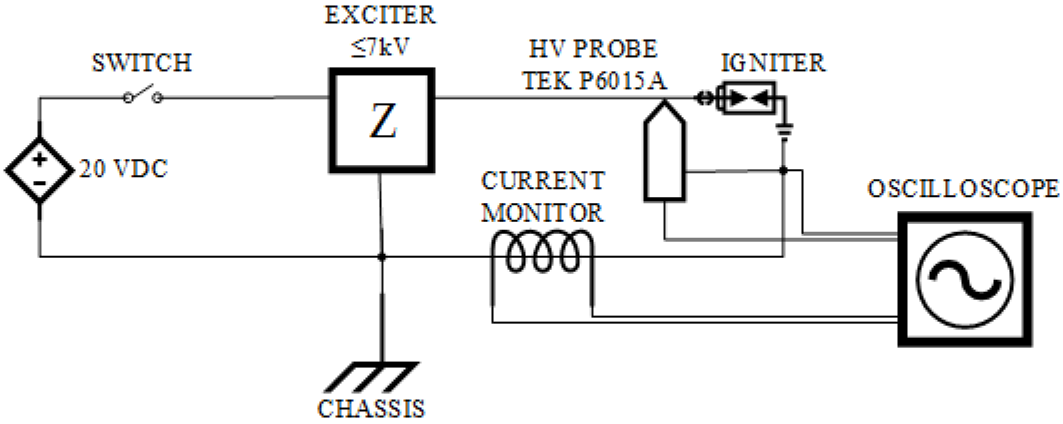

Figure 15 Electrical schematic with instrumentation for energy measurement.

The voltage and current through the circuit were measured using a high voltage probe (Tektronix P6015A) and inductive current monitor (Pearson 6600) connected to an oscilloscope

(Lecroy HDO 4034A) as shown in Figure 15. The electrical energy was measured with the igniter installed in an experimental combustor testing facility. Electrical energy was approximately linearly correlated with pressure, ranging from 0.86 to 1.02 J at 300 and 1000 mbar, respectively.

It is noted that a complex three-dimensional flow field with a bulk speed of approximately 3 m/s existed while measuring the delivered energy which was not present in the vacuum chamber used for determining kernel temperatures. Electrical energy deposition has been found to have a slight positive correlation with crossflow velocity [37], but Okhovat [30] found that spark kernel sensible energy in a crossflow of 5.8 m/s (nearly double the bulk velocity present in these electrical measurements) was not statistically different than quiescent conditions.

3.5 Assumptions and Limitations

The results of this work are based on the following assumptions:

- The kernels are composed strictly of air containing the measured concentrations of H_2O and CO_2, with normal levels of dissociation (no dissociation due to plasma).
- The temperature of the heated backplate is constant during the 9 ms timeframe from the first background image to the last kernel image.
- The H_2O and CO_2 concentrations are constant throughout the duration of testing for each test day.
- The ambient temperature is 300 K (for the sensible energy calculation).
- There is no interference from stray infrared radiation.
- The performance of the ignition system was constant (the igniter was allowed to produce several sparks prior to initiation of data collection to allow time to reach equilibrium).

The results of this work, and the conclusions drawn from them, are restricted by the following limitations:

- All results and conclusions are only valid for quiescent conditions.
- All results and conclusions are only valid within the range of pressures observed.
- Specific temperature and sensible energy results are only valid for this ignition system (including igniter, exciter, and wiring).
- Temperatures determined in this work are the average temperature for the line-of-sight path through the detected kernels.

3.6 Evaluation of Technique

This section describes the efforts that were made to evaluate the inverse deconvolution technique used in this work.

3.6.1 Comparison with Known Temperature

The efficacy of the inverse deconvolution technique was evaluated by comparison of deconvoluted temperatures with temperature measurements collected using a thermocouple above a flame anchored to a McKenna burner. The McKenna burner is well studied and produces a uniform flame that is often used for calibration [43,44]. The burner produces a premixed flame above a circular porous media section, and has an inert coflow sheath to reduce the effects of cross currents on the flame. A mixture of methane and air was supplied to the burner, and nitrogen was used as an inert coflow. Only lean equivalence ratios $\Phi = 0.7$, 0.8, and 0.9 were measured, to allow the assumption that the products consist only of N_2, CO_2, O_2, H_2O, and Ar. NASA Chemical Equilibrium and Applications (CEA) [45] software was used to estimate concentrations to use as inputs for the deconvolution technique. Temperature measurements were taken by traversing a type-B thermocouple over the burner surface starting just outside the coflow sheath, and ending just outside the coflow sheath on the opposite side. Measurements were collected at a height of 4.4 mm above the burner surface, spaced 2 mm apart at the edges of the burner where the temperature changed rapidly with position, and 5 mm apart at the center where the temperature was relatively constant. Temperature profiles measured with the thermocouple are shown in Figure 16. Temperatures reported have been compensated for radiation losses from the thermocouple probe to approximate the true gas temperature [30,46].

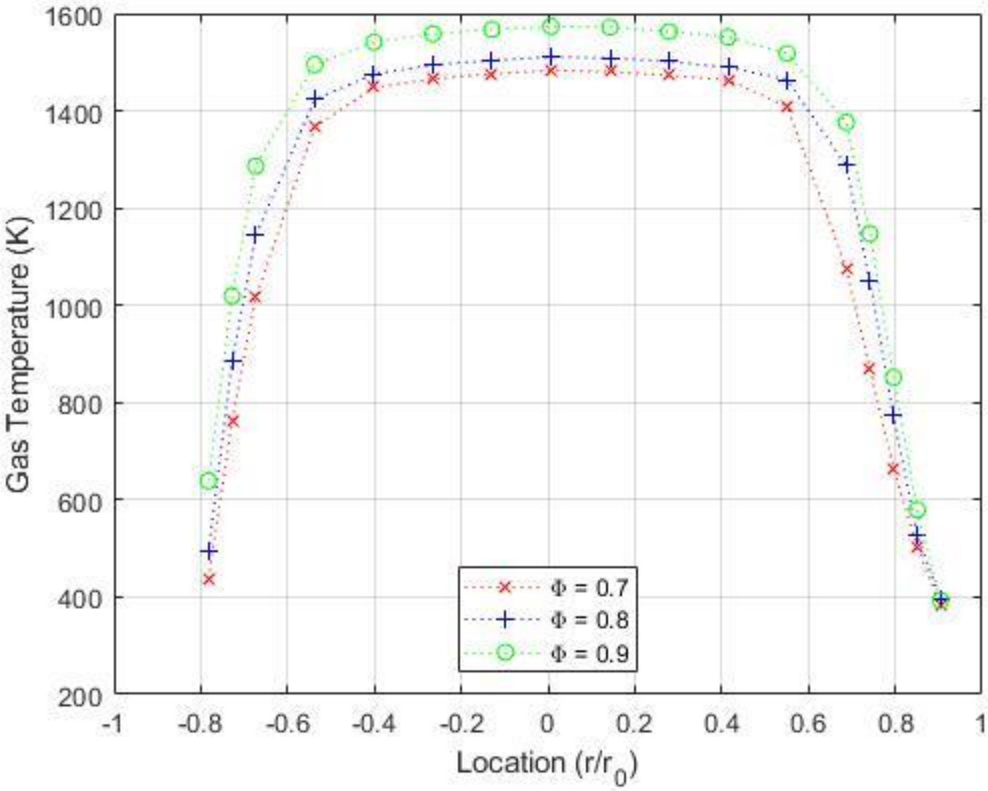

Figure 16 Compensated gas temperature profiles measured with a thermocouple above a McKenna burner.

The infrared camera set up such that its line-of-sight was colinear with the path traversed with the thermocouple. Four data sets were collected at each equivalence ratio, using a filter intended to isolate radiation emitted by CO_2 (bandpass 4370 ± 20 nm). Each data set consisted of 600-800 frames at a rate of 126 Hz and integration time of 0.08 ms. The camera was spatially calibrated using the same method described above.

The iterative inverse deconvolution technique described in Section 3.2 was used to determine the path averaged temperature at the same location as the thermocouple measurements. The deconvoluted temperatures showed reasonable agreement to measured temperatures, with the deconvoluted temperatures being 1-3% greater than the path averaged temperatures measured with the thermocouple, as shown in Figure 17 and Figure 18.

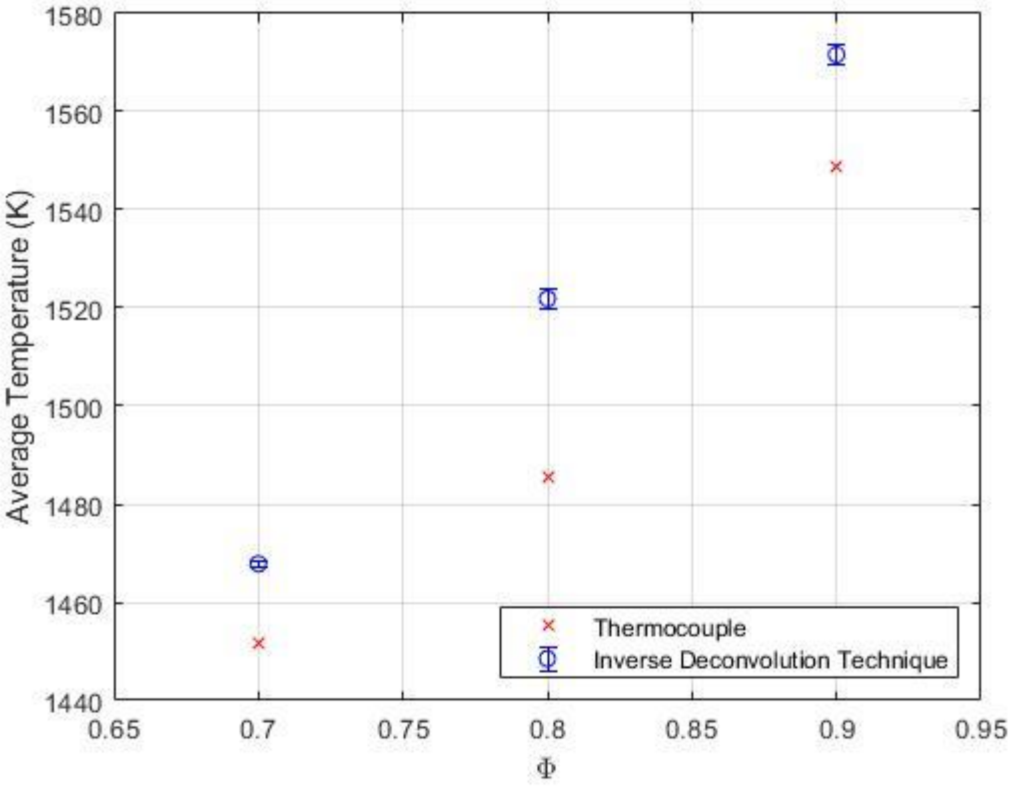

Figure 17 Line of sight path-averaged temperatures measured with the thermocouple and deconvolution technique. Error bars represent the standard deviation of the datasets.

It is noted that due to the 4th power relationship between temperature and intensity, the line-of-sight path-averaged temperatures may be an overestimate. Hotter regions of the line-of-sight path contribute more to the measured intensity than lower temperature regions, and therefore have a greater impact on the path-averaged temperature. The impact of this was evaluated by comparing the algebraic average and the 4th order generalized mean of the of the temperature profile measured with the thermocouple for the $\Phi = 0.7$ case. The algebraic mean and the 4th order generalized mean agreed within 10%.

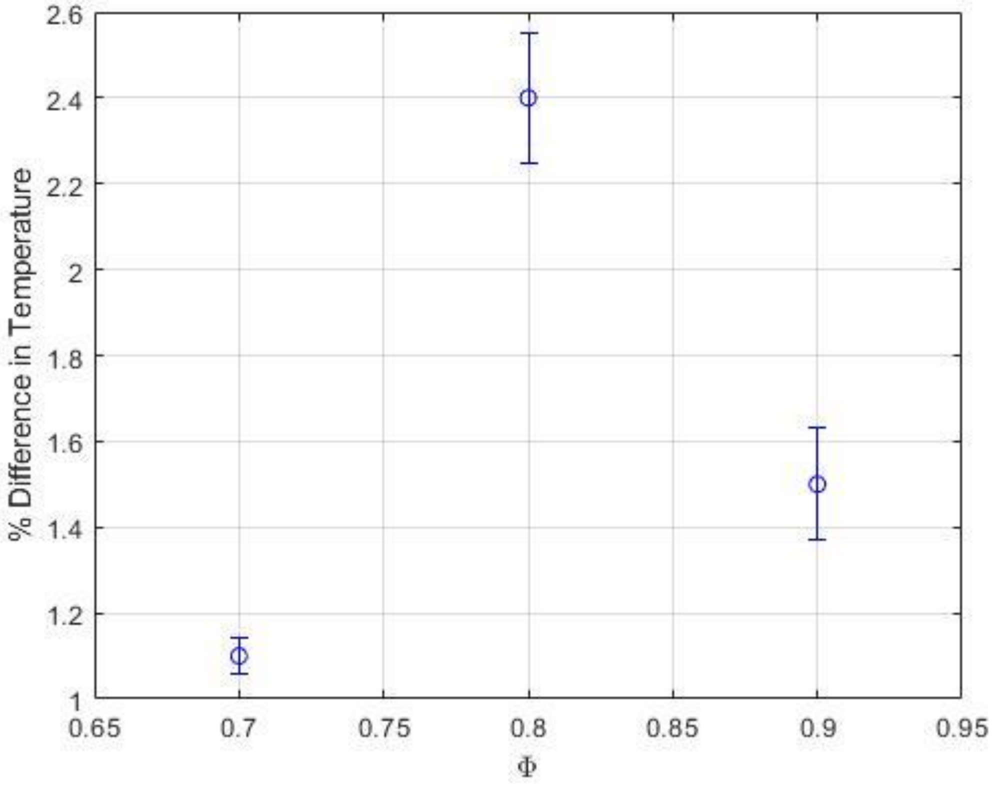

Figure 18 Percent difference between the path-averaged temperatures measured with the thermocouple and deconvolution technique. Error bars represent the standard deviation of the datasets.

An attempt was made to evaluate the technique and the edge detection method at air composition and pressure conditions more similar to those at which sparks were investigated. An apparatus was designed to produce a steady stream of air at 400°C, installed inside the vacuum chamber, and investigated similarly to the McKenna burner. The side-view mirror was included to allow the complete technique to be applied, and the edge detection method to be evaluated. Unfortunately, due to challenges with achieving a hot enough air jet temperature, the signal to noise ratio of emissions from the air jet were insufficient for conclusive evaluation.

3.6.2 Sensitivity Analysis

The sensitivity of the temperatures determined using the inverse deconvolution technique to changes in path length, radiation intensity, CO_2 and H_2O concentrations, and pressure was evaluated. The sensitivity analysis was performed by determining a nominal temperature (i.e. 1290 K) at a typical value for all factors. The analysis was performed using the iterative technique described in Section 3.2. Each factor was then individually perturbed by ±25%, and the corresponding change in deconvoluted temperature was recorded. The results of this analysis are shown in Figure 19. The sensitivity of deconvoluted temperature is not linear with changes in each parameter due to the nonlinear nature of the intensity emissions calculated by the RADCAL model [42].

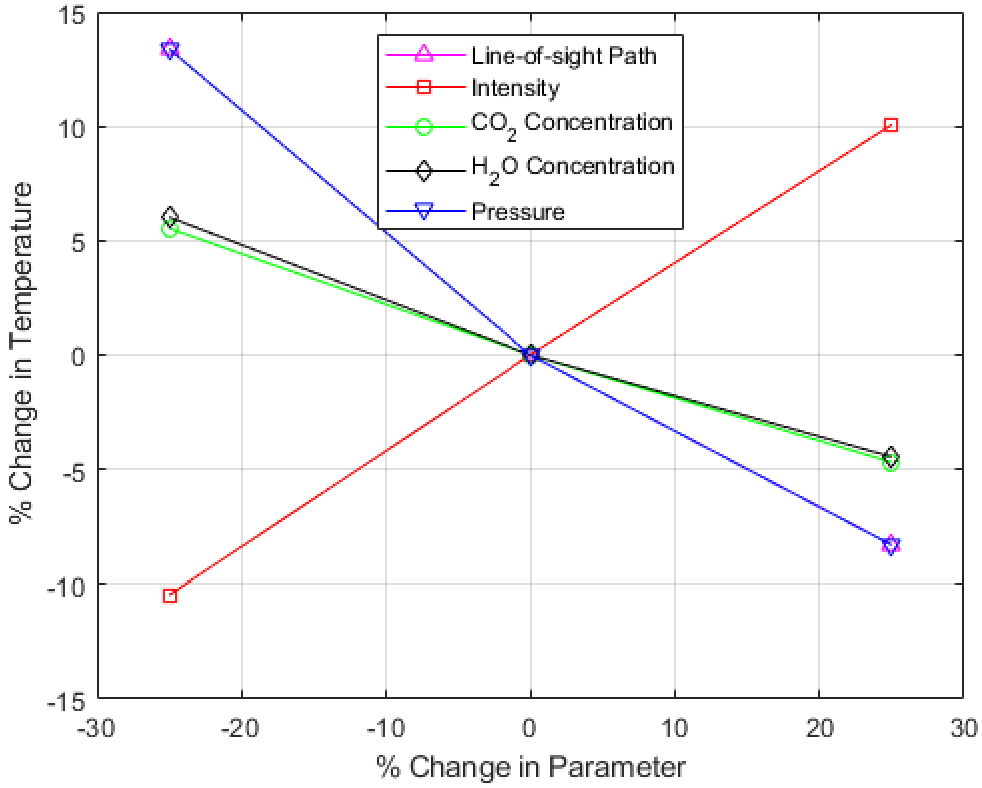

Figure 19 Sensitivity analysis results for the inverse deconvolution technique.

Increasing the CO_2 and H_2O concentrations by 25% caused a decrease in deconvoluted temperature of 5%, while decreasing the concentrations by 25% caused an increase in deconvoluted temperature of 6%. The inverse relationship between temperature and CO_2 and H_2O concentrations is due to changes in the emission and absorption coefficients. Increasing the concentrations of these species increases the emission and absorption coefficients, causing a higher calculated temperature for the same measured intensity.

The technique was found to be most sensitive to decreases in pressure and path length. Temperature sensitivity to pressure and path length were identical, with a 25% increase in both parameters causing an 8% decrease in deconvoluted temperature, and decreasing both parameters by 25% caused a 14% increase in deconvoluted temperature. The pressure dependence of the deconvoluted temperature is due to the same phenomenon as the dependence on CO_2 and H_2O concentrations. Decreasing the pressure leads to lower gas densities, and therefore lower volumetric concentrations of emitting gases. The path length following an identical trend to the pressure is attributed to a similar change in the quantity of emitting molecules for changes in both pressure and path length.

The deconvoluted temperature was found to be positively correlated with intensity, with a 25% increase in intensity leading to a 10% increase in deconvoluted temperature, while a 25% decrease in intensity caused an 11% decrease in deconvoluted temperature. All else remaining constant, an increase in intensity necessitates an increase in temperature due to the inherent relationship between these quantities.

3.6.3 Uncertainty Analysis

An estimate of the uncertainty in deconvoluted temperatures precision and bias errors in the measurements of integrated intensity, pressure, path length, and H_2O and CO_2 concentrations used for determining temperature. The uncertainty for pressure, H_2O, and CO_2 measurements considered manufacturer published instrument accuracies and precision uncertainty. The pathlength uncertainty considered the spatial resolution and an edge detection threshold sensitivity study. The intensity uncertainty included uncertainty from the blackbody calibration and the calibration curve fit. The uncertainty in deconvoluted temperature due to the uncertainty of each parameter was determined using the inverse deconvolution technique and applying sequential perturbation [47] . The resulting temperature uncertainties from each error source were combined using square root of the sum of their squares (RSS) [47]. Details of the sources of error considered for each measurement can be found in Appendix C.

The uncertainty of intensity was dependent on the measured intensity. Therefore, a table of temperature uncertainty based on the measured intensity uncertainty combined with the uncertainties of the other error sources was created for each of the intensity calibration points, as shown in Table 2. The intensities in the table are shifted by the background intensity level to account for background subtracted radiation from the heated backplates. The temperature uncertainty of each pixel was interpolated from this table once temperatures were determined. In short, Table 2 shows representative measured intensities after subtracting the background intensity level, the temperature associated with that intensity, and the uncertainty of the deconvoluted temperature.

Table 2 Uncertainty in deconvoluted temperature as a function of measured intensity.

Intensity (W/m2-sr-um, background subtracted)	Corresponding Temperature (K)	Temperature Uncertainty (K)
0.00	300	379.4
7.39	1361	106.0
18.69	2225	148.4
35.17	4202	427.2

3.7 Improvements Compared to Previous Works

At the request of the committee, this section has been added to describe improvements to the experimental technique developed by Blunck et al. [17] and Okhovat [30] that were developed over the course of this work.

3.7.1 Pressure

As was the goal of this work, the IR inverse deconvolution technique was applied to determine spark kernel temperatures at subatmospheric pressures. Observations of subatmospheric pressure required the use of a vacuum chamber. The vacuum chamber already existed but did not have a suitable window for infrared measurements. Significant effort was made in the design and selection of a suitable window, which satisfied the conflicting requirements of IR transmissivity, cost, strength, and size, as discussed in Section 3.1. Minor modifications were also made to the database generation concept to allow for pressure to be varied.

3.7.2 Edge Detection

Several edge detection alorithms were evaluated, as discussed in Section 3.3.3. A binarization threshold was selected as the best method, similarly to that used by Okhovat [30]. However, a different definition for the binarization threshold was used, as discussed in Section 3.3.3.

3.7.3 Uncertainty Analysis

This work expanded significantly on the uncertainty analysis of both Okhovat [30] and Blunck et al. [17]. Previous works considered only the sensitivity of the deconvolution technique to representative but arbitrary perturbations in the input parameters. This work includes a similar analysis in Section 3.6.2, and expands on this analysis with a thorough estimation of the measurement uncertainties of each parameter, as described in Section 3.6.3 and Appendix C.

3.7.4 Analysis Software

Previous work by Okhovat [30] and Blunck et al. [17] laid a strong methodology foundation on which to build. Previous analysis software relied heavily on manual data manipulation and frequent script modifications and manual value entries within the script, which is prone to human error. Analysis software was developed in this work which automates most of the data manipulation and manual entries. The only manually entered values in the analysis software developed in this work are analysis parameters and inputs, such as the binarization threshold criteria.

3.7.5 Sensible Energy Calculation

Previous works assumed constant specific heat and a change in temperature to determine sensible energy. The specific heat of air varies by more than 25% over the temperature range in question and is therefore not an ideal method of determining the sensible energy of spark kernels. This work uses enthalpy to determine the sensible energy within the kernels, which accounts for the large variability in the specific heat with temperature.

3.7.6 Test Article

Due to shared nature of the vacuum chamber, there was a need to be able to quickly set up and align the igniter, mirror, and camera. An alignment jig was designed and fabricated, as described in Section 3.1. Using this jig, the experiment could be installed and aligned in approximately 1-2 hours. The jig is also adaptable for future use.

3.7.7 Electrical Measurements

This work improved upon the electrical measurements of Okhovat [30] by measuring the high voltage electrical energy delivered to the igniter, rather than the low voltage energy delivered to the exciter. The exciter consumes significant energy, which impacts the comparison between supplied electrical energy and kernel sensible energy. Okhovat measured approximately 10 J supplied to the exciter, while in this work the energy delivered from the exciter to the igniter was 1.02 J at atmospheric pressure.

3.8 Boundary Conditions for a Numerical Model

This work did not include a numerical model. However, the results produced could be used to validate a model if one were to be created. The following is a list of boundary conditions that should be considered if making a numerical model based on this experiment:

- Igniter geometry
    - Igniter outer diameter: 12 mm
    - Anode inner diameter: 6 mm
    - Cathode diameter: 3 mm

  - Sunken tip geometry: The insulator is approximately 0.5 mm step into the igniter tip relative to the anode, and the cathode is another 0.5 mm step into the tip.
  - Cooling holes: 12x 1mm holes arranged in a 10mm circle
- Spark characteristics
  - Electrical energy supplied (see Sections 3.4 and 4.3.)
  - Spark duration is not known, so it is recommended to approximate the spark as an instantaneous energy deposition.
  - Sparking frequency (may impact electrode temperature): ~2.6 Hz
- Ambient conditions
  - Nearest vacuum chamber wall was 15 cm away
  - Pressure: 300, 380, 450, 750, 1000 mbar
  - Quiescent air
  - Ambient temperature of 300 K

Chapter 4 Results and Discussion

This chapter presents the results from experiments, and includes a discussion of the trends observed, applications of the findings to practical systems, and comparison of the results to literature. First, the spatial development of spark kernels is discussed, followed by a discussion of kernel temperature evolution and spatial temperature distributions, and lastly the deposited energy and efficiency are reported. Results for kernels at 300, 380, 450, 750, and 1000 mbar are presented. Results for kernels at low pressure (380 mbar), moderate pressure (750 mbar), and atmospheric pressure (1000 mbar) are discussed in greater detail.

The results presented in this work are based on a total of 10,972 spark events. Details of the number of spark events at each pressure and evident after plasma was observed can be found in Table 3. Note that the number of kernels evident after plasma was detected reduces with time as heat is transferred to the surrounding fluid and the kernel becomes no longer evident in the infrared. It is noted that the deconvolution technique assumed that kernel temperatures were at least equal to the ambient air temperature of 300 K, but in practice all detected temperatures were 500 K or greater. Unless otherwise specified, ‘initially,’ refers to the first frame captured by the camera, or 0.67 ms after plasma was detected.

Table 3 Number of kernels detected at each pressure and evident after plasma was detected.

Pressure (mbar)	Time after plasma (ms)					
	0.67	1.33	2.00	2.67	3.33	4.00
300	1816	1816	1800	1555	1299	837
380	2060	2060	2059	1923	1593	1182
450	1954	1954	1952	1864	1588	1232
750	2325	2325	2325	2293	2057	1584
1000	2817	2817	2817	2693	2249	1628
Total	10972	10972	10953	10328	8786	6463

4.1 Spatial Development

This section describes the spatial and temporal development of spark kernels, and how the development changes as the pressure is reduced. Changes in shapes, kernel sizes, and penetration depths are discussed. Infrared radiation emissions are reported because they are useful for visualizing the development of kernels. Note that images of kernel radiation emissions presented are 2-dimensional projections of 3-dimensional participating media. Hence regions with higher radiation emissions can indicate greater line-of-sight depth, greater radiation emissions, or both.

4.1.1 Radiation Emissions

Time-resolved development of representative kernels in the IR are shown in Figure 20. At atmospheric pressure, the kernel initially appears as an arrowhead shape, with a narrower region of lower intensity dividing the kernel into two almost symmetric lobes [15,48,49] across a line parallel to the igniter axis (i.e., see the left most column in Figure 20). Regions of peak projected intensity are visible near the center of both lobes, which persist through the entire lifetime of the kernel. Throughout the kernel lifetime, there is an intensity gradient that tends toward lower intensity values near the kernel edges as a result of mixing with surrounding air decreasing temperatures. The kernel's peak and mean intensities decrease with time until it is no longer detected, consistent with a decrease in temperature.

The moderate-pressure (750 mbar) kernel radiation intensity followed a similar trend as the atmospheric pressure kernel, in that both the peak intensity and mean intensity decrease over the life of the kernel (see the middle column in Figure 20). Unlike at atmospheric pressure, the apparent image of the kernel initially contained four connected lobes, symmetric across a line parallel to the axis of the igniter. The upper lobes had higher intensity emissions than the lower lobes, with the upper left lobe being the highest intensity. After 1.33 ms the kernel transitioned into a mushroom shape, with a region of higher intensity contained within the upper lobe of the mushroom. The two lobes of the mushroom shape are visible until 4 ms, and a trailing column is visible until 3.33 ms. A trailing column in the wake of spark kernels was reported by Okhovat [16,30] for a similar igniter, as well as other researchers under different conditions [11–13,33,41]. After 4 ms only the lobe containing the highest radiation emissions can be seen.

At lower pressure (i.e., 380 mbar) the kernel radiation emissions decreased similarly to the atmospheric- and moderate-pressure cases with time (see the right column of Figure 20), but with lower initial intensity values and several notable differences. The low-pressure kernel initially appeared as a mushroom shape with an axis of symmetry that was not parallel to the igniter axis. The motion of the kernel, however, was parallel to the igniter axis based on the kernel locations at later times. An elongated region of higher relative intensity was initially observed in the mushroom shape section of the kernel, extending from the middle into the upper lobe closer to the igniter. By 1.33 ms the majority of the kernel moved away from the igniter, while the lobe closest to the igniter remained stationary but still connected to the rest of the kernel by a thin tendril of hot gas. By 2 ms the kernel bifurcated into two separate regions. The majority of the kernel traveled further away from the igniter while the lobe closer to the igniter tip remained stationary through the kernel lifetime. In contrast, the kernels at both atmospheric and moderate pressure remained intact and moved cohesively away from the igniter. Additionally, the low-pressure kernel traveled further from the igniter in the same amount of time than the atmospheric- and moderate-pressure kernels, indicating a higher velocity.

In both the atmospheric- and low-pressure kernel images there are small regions of high intensity that move independently from the kernels. These regions are material ablated from the igniter during the spark event. Both this work and Okhovat [30] found that material ablated from the igniter intermittently at atmospheric pressure. At lower pressures the frequency of ablation increased, and at pressures of 450 mbar and below, nearly all kernels were accompanied by ablated material.

It should be noted that while Figure 20 shows kernels after 4 ms, the intensity measured beyond 4 ms was for most kernels below the limit used for edge detection as discussed in Section 3.3.3. The dynamic color range used in Figure 20 broadens the differences in intensity in order to more clearly display the general shapes of the kernels. The increased level of background noise in the images at later times alludes to the low radiation intensity emitted by the kernels relative to the background radiation emissions.

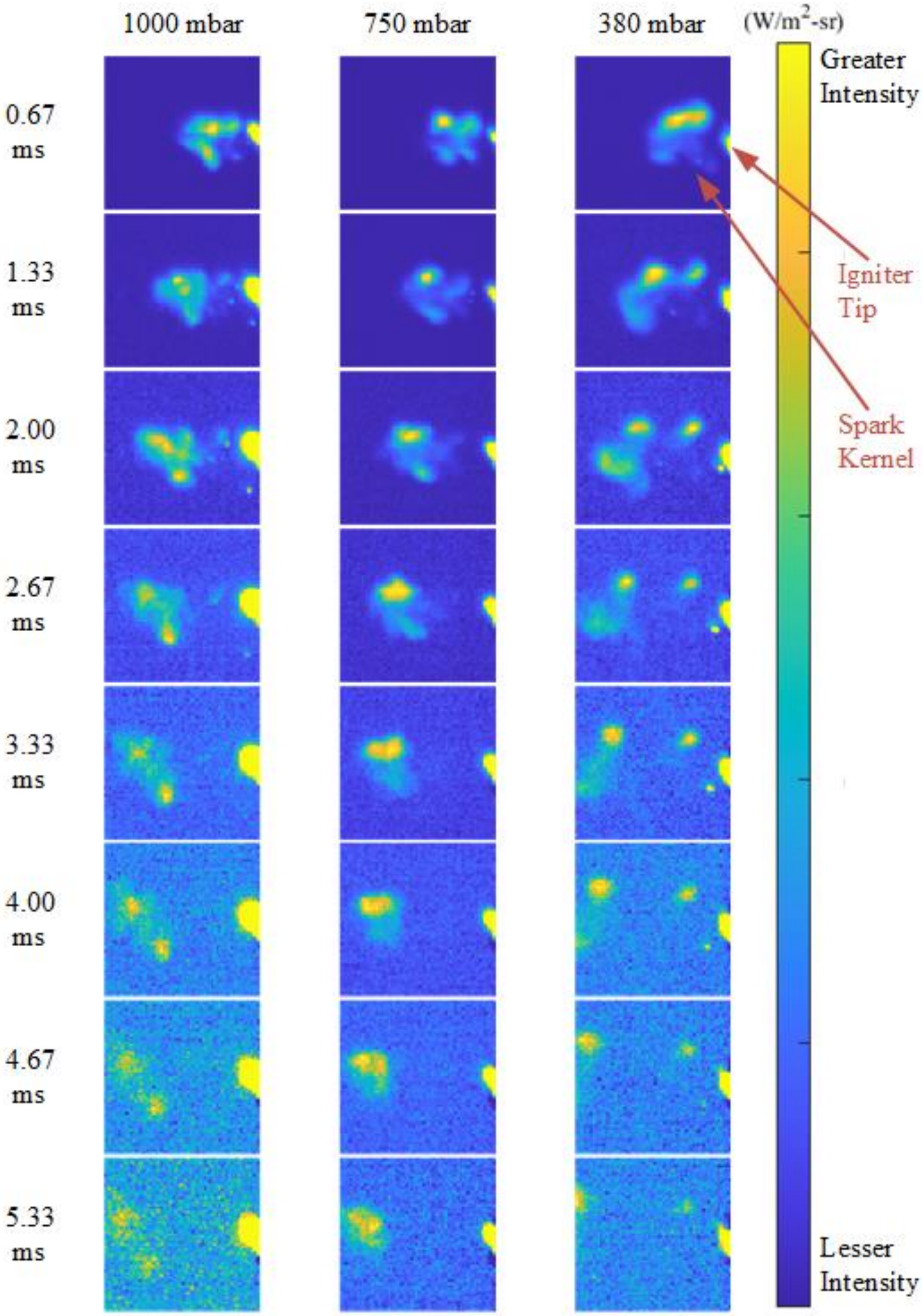

Figure 20 Infrared images of representative kernels produced in air at 1000, 750, and 380 mbar. These images have dynamic color ranges (ignoring radiation from the igniter tip) in order to better show the relative intensities of the kernel in each image.

Images of the average kernel radiation emissions for all kernels at 380, 750, and 1000 mbar over the kernel lifetimes are shown in Figure 21. At atmospheric pressure the average apparent shape of the kernel after 0.67 ms is arrowhead or jet shaped, similar to findings of Okhovat [16,30] and the representative kernel described earlier. The average kernel has a region of higher radiation intensity forming two lobes, with a higher intensity upper lobe and an intensity gradient that tends toward lower intensity near the kernel edges.

At 750 mbar and 0.67 ms after plasma, the average kernel had two lobes that are roughly symmetric. The upper lobe emitted more radiation than the lower lobe and had a gradient toward lower intensity at the edges, as was also observed at atmospheric pressure. The lobes were more rounded at 750 mbar compared to the kernels at atmospheric pressure, and do not resemble an arrowhead.

The kernel average at 380 mbar, as with the representative kernel at the same conditions, had several lobes of high intensity surrounded by a region of lower intensity. The average low-pressure kernel had higher intensity in the center and lower intensity at the edges, as in both the atmospheric- and moderate-pressure kernels. The low-pressure kernel appears even more rounded than the moderate-pressure kernel.

After 1.33 ms kernels at all pressures elongated away from the igniter, and the low-pressure kernel begins to show necking. After 2 ms the atmospheric- and moderate-pressure kernels elongated further away from the igniter, but with a narrower region approximately one diameter wide extending back toward the igniter. The lowest-pressure kernels on the other hand bifurcated into two separate regions by 2 ms. At later stages (i.e. 2.67 to 4 ms), the trailing column of atmospheric- and moderate-pressure kernels faded from detection, while both regions of the low-pressure kernel remained visible. Kernels at all three pressures formed into crescent shapes as they moved away from the igniter. At the lower pressure, the region that was closer to the igniter remained stationary through the kernel lifetime, similar to results for the corresponding time-resolved kernel shown in Figure 20.

At all pressures the average kernel maximum radiation intensity, mean radiation intensity, and the difference between the maximum and average intensities decrease over the kernel lifetime. From 1.33 ms to the end of life, kernels at 1000 and 750 mbar take on similar shape features, and are mostly uniform in intensity with the exception of a region of elevated intensity shaped like a chevron aiming away from the igniter tip. The kernel average at 380 mbar differs in that it has split into the moving and stationary regions.

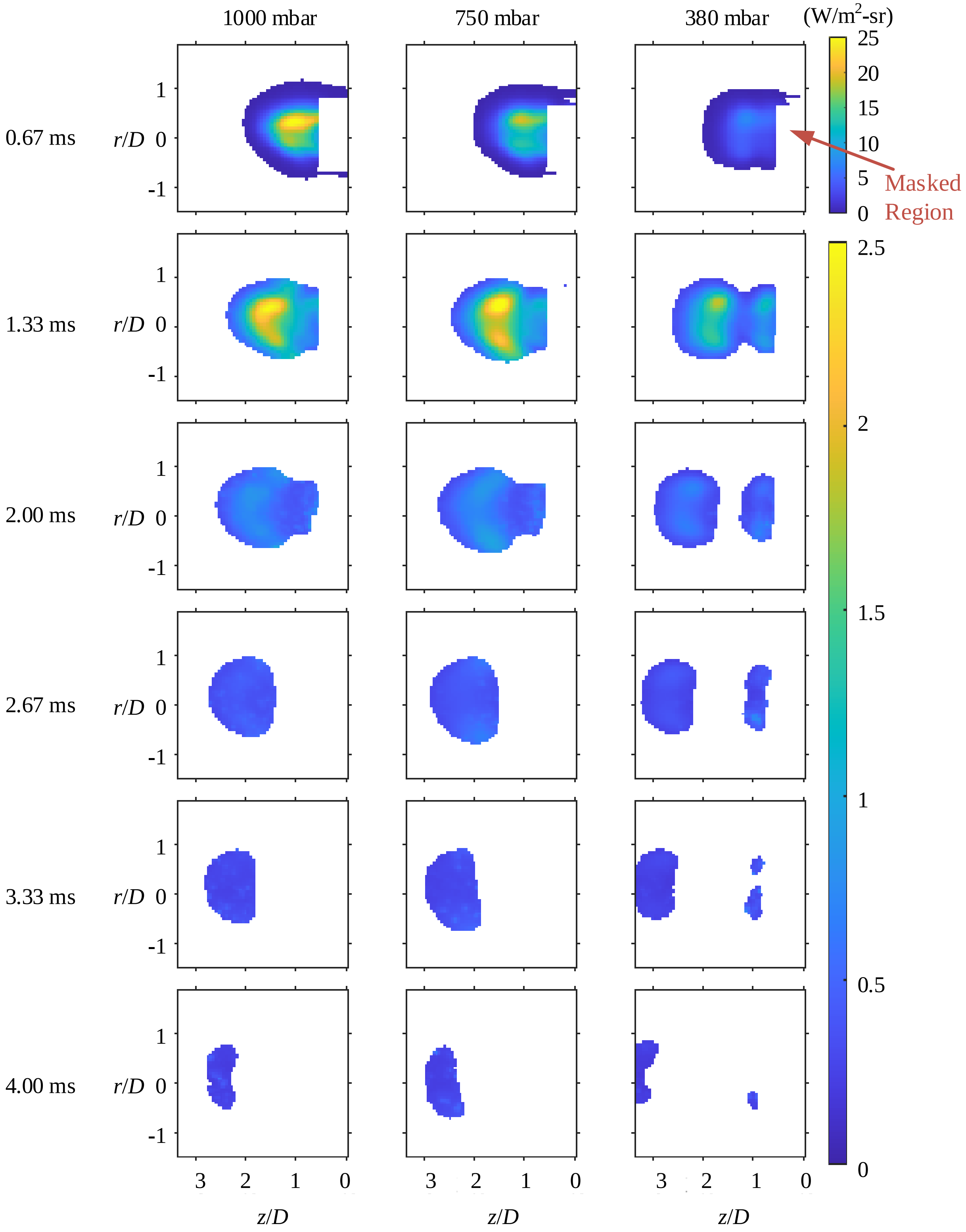

Figure 21 Time-resolved average intensity images for all kernels at 1000, 750, and 380 mbar.

Figure 22 illustrates the reasoning for describing the kernels as vortices. Kernels at all pressures and times after plasma have greater line-of-sight path lengths in the center of the kernels, and shorter path lengths at the kernel edges. This path length distribution, with high values in the center and lower values at the edges, combined with the higher apparent intensity lobes in kernels at all pressures, is indicative of the formation of the kernel into a toroidal shape, or a puff, similar to findings reported by others [11–16,30,33,41].

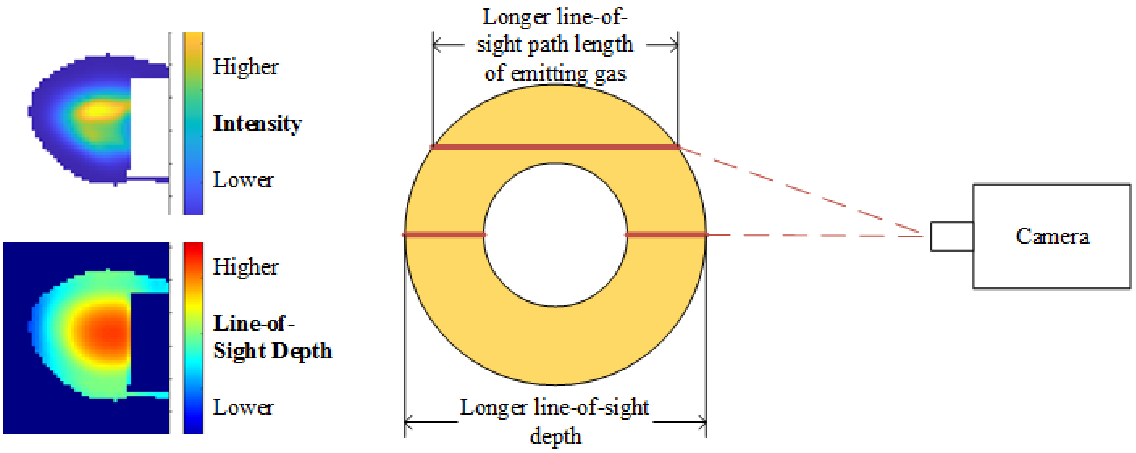

Figure 22 Comparison between line-of-sight depth (bottom left panel), apparent kernel intensities (top left panel), and path lengths through a toroidal region of emitting gas (shown in yellow).

4.1.2 Expected Kernel Location

Igniter position within a combustor is an important design consideration. Factors such as equivalence ratio, air temperature, and air velocity are typically nonhomogeneous inside GTE combustors. As a result, it is important to ensure the spark energy is delivered to a region where the conditions can support ignition. To understand where kernels are likely to exist relative to the igniter, maps of how frequently radiation emitted by kernels was detected are shown in Figure 23.

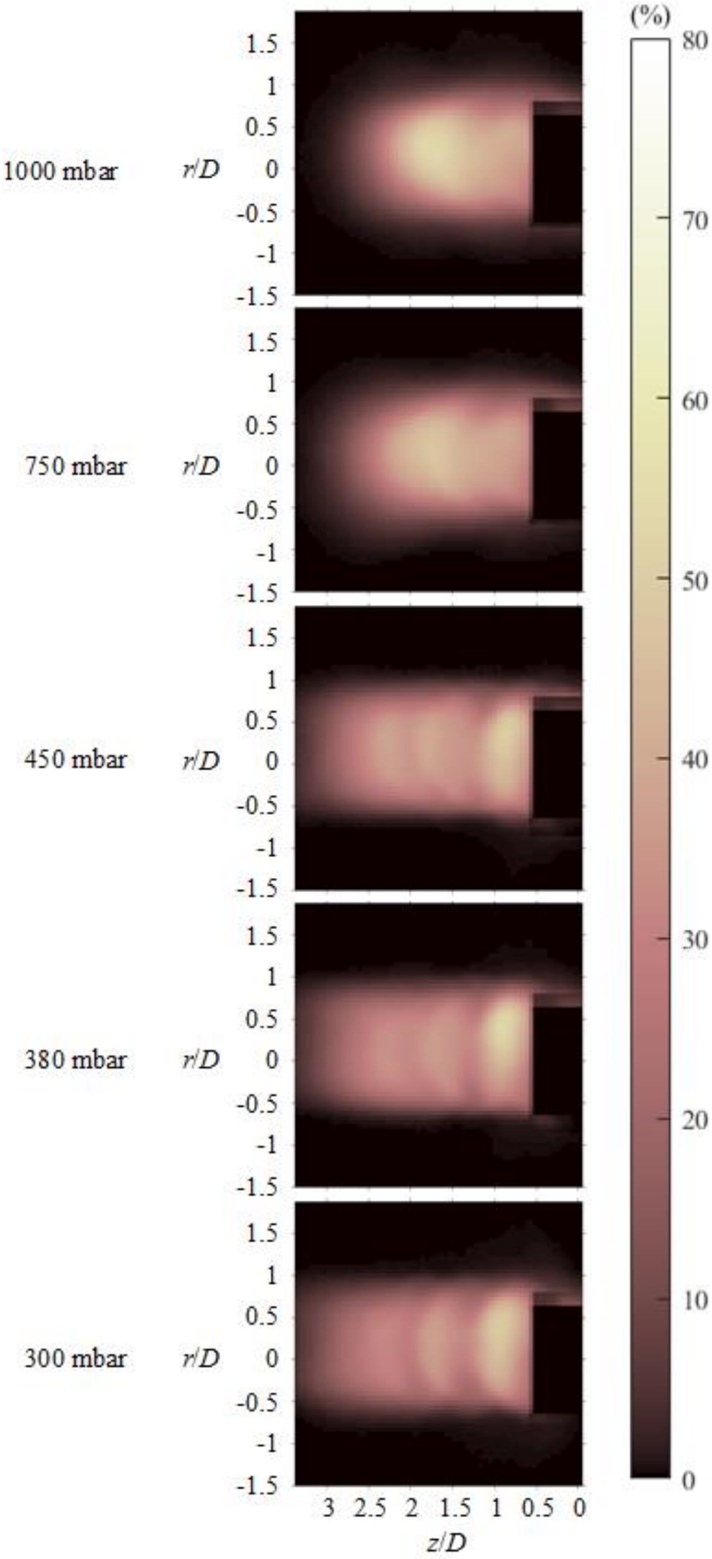

Figure 23 Maps showing how frequently radiation from spark kernels was detected at all pressures interrogated.

The axial width of the kernel path envelopes is similar at all pressures. Radiation from kernels was detected at least 10% of the time within a region extending 0.9 diameters above, and 0.6 diameters below, the igniter axis. The off-axis distribution of kernel position is attributed to preferential arcing of plasma in one location of the annular electrodes. This is anecdotally evident by uneven wear of the igniter electrodes.

Kernels at lower pressures (i.e. 300-450 mbar) penetrated further from the igniter than kernels at moderate and atmospheric pressure (i.e. 750 and 1000 mbar). At atmospheric and moderate pressure, kernels were detected at least 10% of the instances as far as 2.6 diameters from the igniter tip, while at lower pressure kernels were detected 3.2 diameters from the igniter tip. Since kernels at all pressures were detectible for similar durations (i.e., up to 4 ms), this suggests that moderate- and atmospheric-pressure kernels had greater residence time within 2.6 diameters from the igniter tip, while kernels at lower pressure have greater penetration depth and velocity. Average kernel velocities based on these penetration depths and times are 7.8 and 9.5 m/s at 1000 and 300 mbar, respectively.

Another difference between atmospheric/moderate pressure and low pressures is the presence of ‘rings’ of high and low position frequency at low pressures. These rings are an artifact of the discrete times at which the camera captured radiation emissions. The presence of these rings at low pressures indicates that the low-pressure kernels were traveling at higher velocity than at atmospheric and moderate pressure.

Okhovat [30] reported that kernel trajectories tended to spread out widely from the igniter based on apparent kernel centroid locations, while in this work kernels were primarily detected within a cylindrical region off the igniter tip. This discrepancy is attributed to differences in the way kernel motion is displayed by apparent centroids (as reported by Okhovat), which are single points, and 2-dimensional location frequency (as reported in this work).

4.1.3 Evolution of Kernel Volume

The evolution of kernel volume at all pressures is shown in Figure 24. Kernels at all pressures are roughly 3.7 cm^3. Kernel volumes decreased at approximately 1.1 cm^3/ms until the kernels were no longer detected. From 2.67 to 4 ms, the volume of the 300-mbar kernels decreased at a faster rate and were only just detectable by 4 ms. Ambient air is entrained into the kernels, causing them to expand. However, the apparent kernel volume decreases with time as the entrained air lowers their temperature and heat is dissipated to the surroundings.

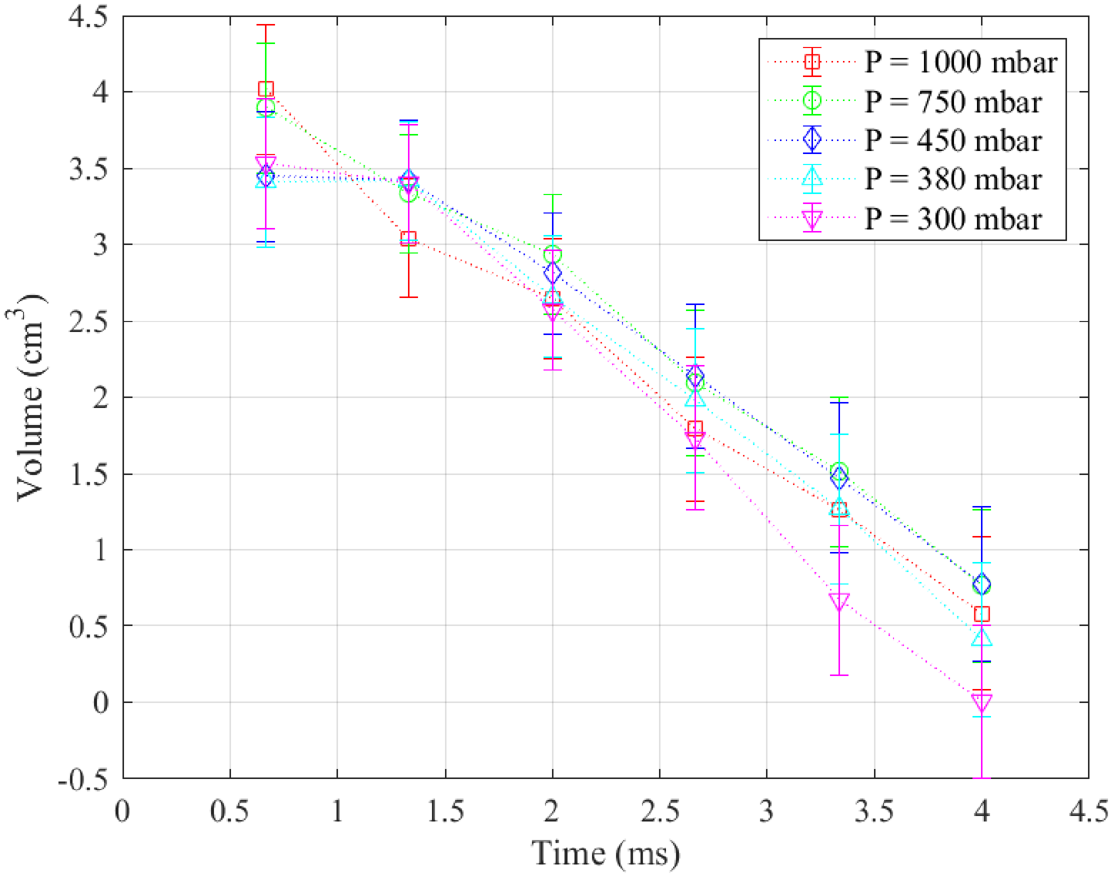

Figure 24 Temporal evolution of the volume of spark kernels at varying pressures. Error bars represent systematic and precision uncertainty.

4.2 Temperature Results

This section presents the temperature evolution of spark kernels at varying pressure. The temperature distributions are reported for the same representative kernels first presented in Section 4.1.1, followed by the evolution of the a

K,[verage temperature distribution, spatial distributions of the average and peak temperatures, and the evolution of the volumetric-average temperatures for kernels at all pressures. All temperatures reported are path-averaged as previously noted.

4.2.1 Representative Temperatures

The temperature development of representative kernels are shown in Figure 25. The kernels at all pressures had higher temperature lobes in the center, and a gradient to lower temperatures at the kernel edges. This is consistent with the representative radiation intensity emissions reported earlier. Until 2.67 ms after plasma, the shape of the kernels in the temperature images are consistent with the intensity images. From 3.33 ms to 4 ms the intensity images show regions of radiation emission that is not represented in the temperature images. The excluded radiation was not processed because the magnitude of the intensity was less than the detection threshold (e.g. 0.2 W/m^2-sr) described in Section 3.3.3.

At atmospheric pressure (see the left column of images in Figure 25), the peak temperature was initially 2500 K but reduced to 1200 K by 1.33 ms. Throughout the kernel lifetime there were small regions of higher temperatures. As discussed in Section 4.1, the kernel temperature decreases as cool air is entrained into the kernel.

At moderate pressure (see the middle column in Figure 25), the peak temperature is near 4000 K and reduces to 1800 K by 1.33 ms. Regions of higher temperature corresponding to the higher intensity regions are visible until 2.67 ms. At lower pressure (see the right column in Figure 25) the peak temperature is 2200 K, which is lower than the atmospheric kernel. As was also shown in the intensity image, the low-pressure kernel bifurcated by 2 ms. The atmospheric kernel is initially larger than both the moderate-pressure and low-pressure kernels, but by 1.33 ms kernels at all three pressures are similar in size. Temperature trends are further discussed in the next section.

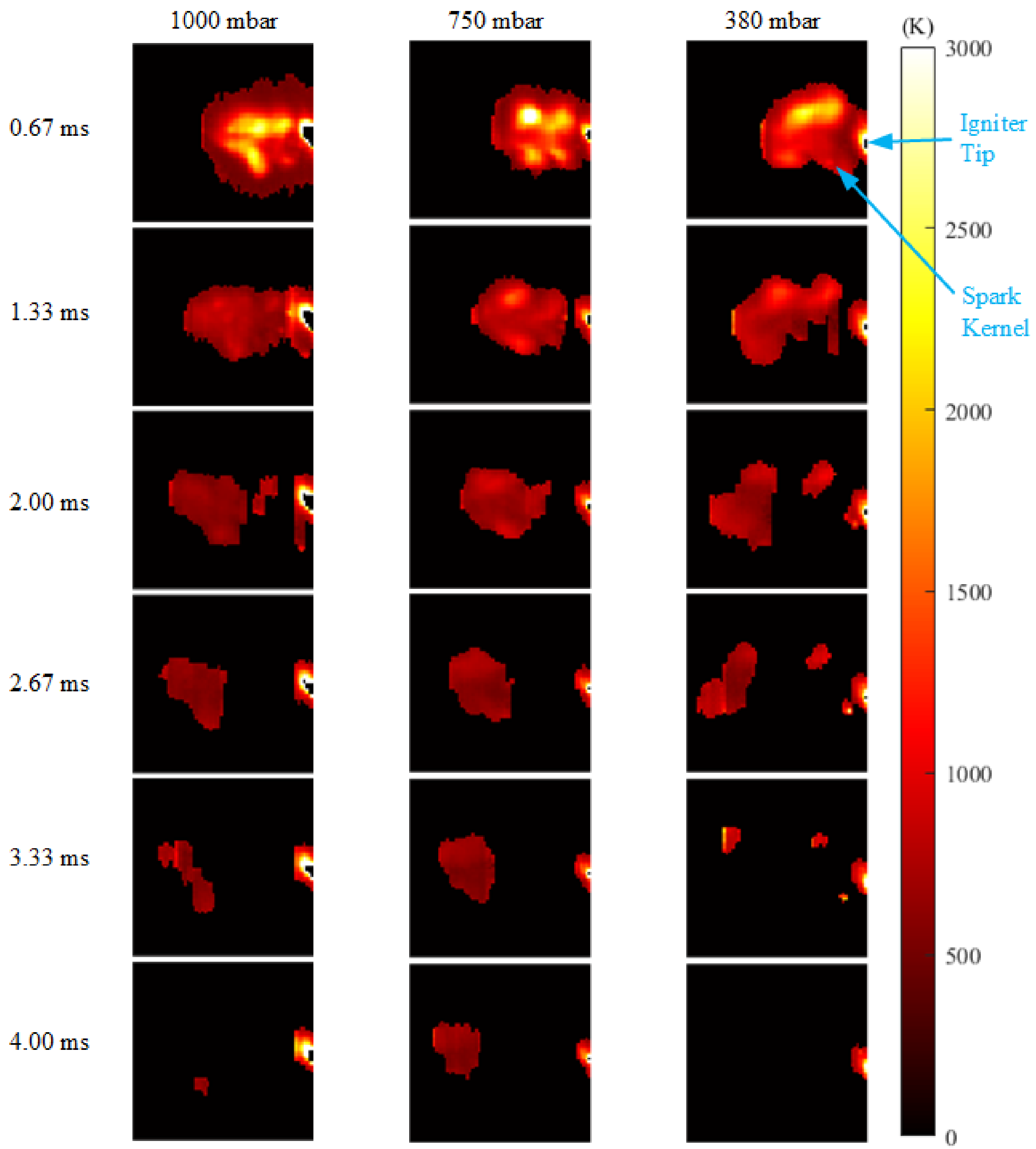

Figure 25 Temperature images for representative kernels at 1000, 750, and 380 mbar conditions.

It is noted that the average temperature of the low-pressure kernel increased between 2.67 and 3.33 ms. Given that there was no input of energy during this time, it was not possible for the maximum gas temperatures to increase. However, the path averaged temperature did increase because the kernel volume decreased to only include gases that were hotter on average. This observation is further discussed in Section 4.2.4.

4.2.2 Phase-Averaged Temperature Distribution

The phase-averaged temperature distributions (i.e. the time-resolved average temperatures) are shown in Figure 26. At all pressures, the shapes and temperature distributions shown in Figure 26 were similar in relative magnitude to their corresponding average intensities shown in Figure 21. The kernels initially had higher temperatures in the center lobes and a gradient toward lower temperature at the kernel edges. The moderate-pressure kernels had the hottest maximum temperature (2100 K), followed closely by the atmospheric-pressure kernels (2050 K), and the low-pressure kernels had the lowest maximum temperature (1800 K). The minimum average temperatures, in contrast, were initially the highest at low pressure, with kernel edge temperatures of 750, 560, and 550 K at 380, 750, and 1000 mbar, respectively. Kernel temperatures were therefore more varied at atmospheric and moderate pressure, and more uniform at lower pressure. Successful ignition is dependent on obtaining sufficient temperature; lower maximum temperatures at lower pressures may help explain some of the challenge with ignition at high altitude.

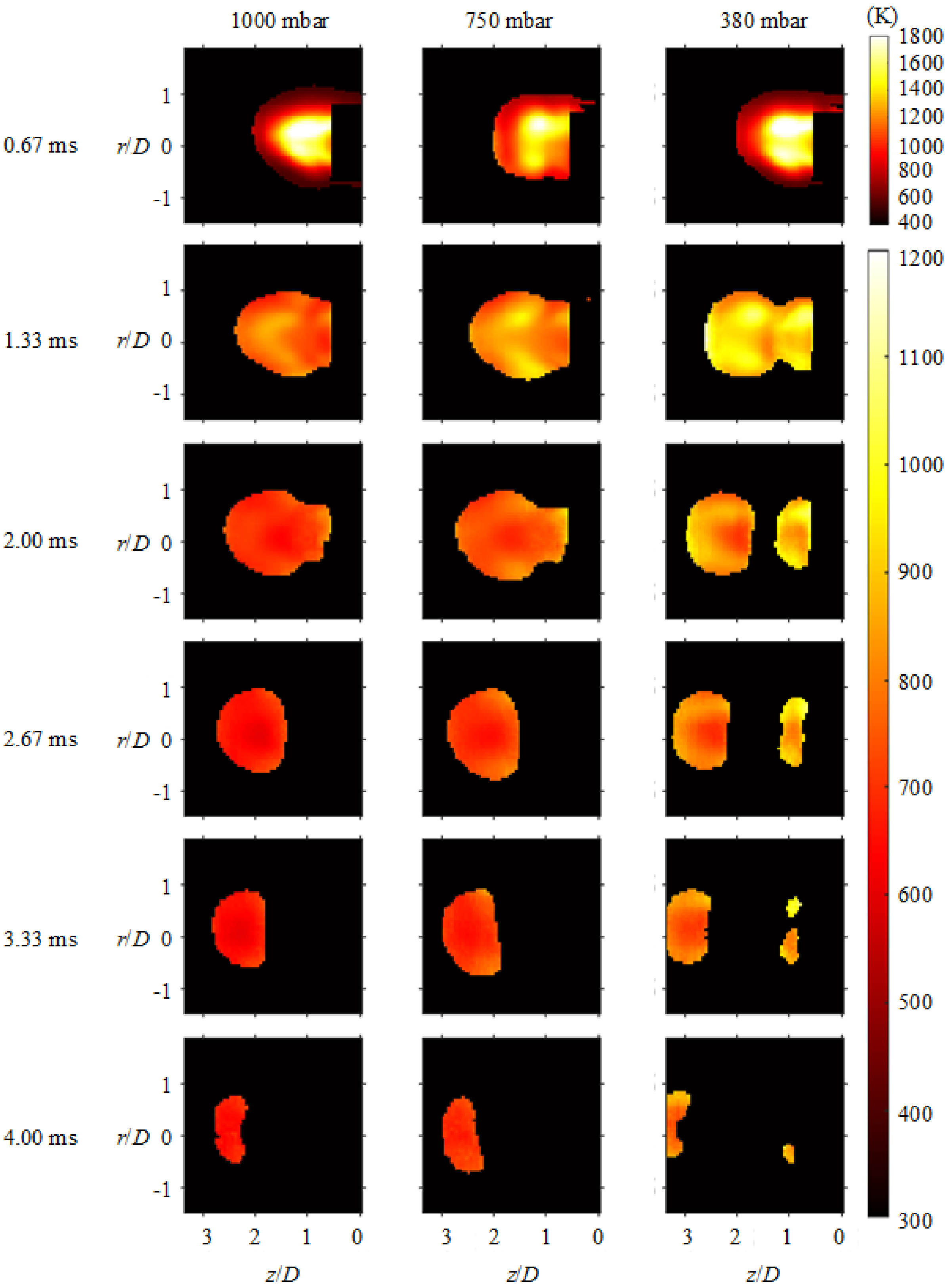

Figure 26 Phase average temperature images for all kernels at 1000, 750, and 380 mbar.

It is plausible that the pressure dependence of the temperature distribution of spark kernels is caused by differences in the spark discharge characteristics at different pressures. Arc discharges are more efficient at converting electrical to thermal energy than glow discharges. Some works used specially designed and tuned ignition systems to maximize the ratio of arc to glow discharge [28,37]. This work used a production ignition system which did not have a way to tune the spark characteristics. Additionally, the ignition system used here was triggered passively when the voltage applied to the spark gap exceeded the breakdown voltage [35]. Therefore, the spark characteristics for the ignition system used in this work may be pressure dependent due to the pressure dependence of the breakdown voltage of air. If the spark was predominantly a greater ratio of arc to glow at atmospheric pressure than at low pressure, this could explain both the decrease in efficiency and the increase in temperature uniformity at lower pressures. Glow discharges are proximal to the cathode resulting in high heat loss to the cathode. Glow discharges are also longer in duration, allowing more time for heat transfer within the kernel to even out the temperature [18,37].

The temperature distributions of kernels at all pressures were more uniform at 1.33 ms than 0.67 ms. Maximum temperatures decreased, and minimum temperatures increased. The maximum temperatures reduced to 1080, 950, and 870 K, at 380, 750, and 1000 mbar, respectively, while the minimum detectable temperatures increased to 800, 680, and 660 K. The decrease in maximum temperature is attributed to thermal diffusion to the cooler regions of the kernels, and entrainment of cool surrounding air into the kernels. The increase in minimum detectable temperature is attributed to heat transfer from the hotter regions of the kernel and, given that the apparent kernel volume decreased, cooling of the air at the kernel edges below the detection threshold.

The temperature distribution at all pressures changed such that the kernel edges were hotter than the center by 2 ms after plasma. This shift is attributed to ambient air being entrained by the vortex into the center of a kernel, as illustrated in Figure 22. The change in the temperature distribution highlights the relatively significant role that mixing and entrainment have on the evolution of spark kernels.

The moving region of the bifurcated kernels at low-pressure cooled at a faster rate than the stationary region. For example, maximum temperatures in the moving region decreased to 970 and 850 K at 2 and 2.67 ms, respectively, while maximum temperature in the stationary region decreased to 1000 and 970 K. The higher rate of cooling of the moving portion of the kernel is consistent with greater entrainment and mixing with cool ambient air than the stationary portion of the kernel. This difference in entrainment may alter the way fuel and oxidizer are mixed in the ignition zone of a combustion system and may affect the early stages of flame propagation.

It is noted that Okhovat [30] reported maximum path-averaged kernel temperatures of 1200 K at 1 atm, while in this work the maximum path-averaged temperatures were 2050 K at similar conditions. This discrepancy in temperature is attributed to two factors. First, this work used a different edge detection threshold (see Section 3.3.3), which resulted in shorter path lengths than the work of Okhovat [30]. Shorter path lengths result in higher temperatures. The second, and likely more impactful, difference is in the circuitry connecting the igniter to the exciter. The same exciter and a similar igniter (i.e. the same model) were used by Okhovat and in this work, but different connecting wire was used. The electrical configuration of an ignition system can have significant impact on the spark characteristics [37], and it was found in the course of this work that even small increases in grounding impedance (e.g. 1 ohm) noticeably subdued the spark produced by the igniter. A reduction in the delivered energy by the spark would decrease the resulting sensible energy and temperature. In this work, a minimum length of heavy gauge high-voltage rated wire was used to connect the igniter to the exciter (details provided Section 3.1). The exact wire used by Okhovat is not known. This potential difference can explain the temperature deviation between findings of Okhovat and this work.

4.2.3 Average and Peak Temperature Distributions

Igniter placement is an important design consideration for GTE combustors because conditions such as fuel-air mixture are not homogenous. The igniter must be placed such that the spark kernels are produced in a location where conditions can support ignition. Knowledge of the spatial temperature distribution of spark kernels relative to the igniter can be useful for engineers when designing the placement of igniters within a combustion system. The right column of Figure 27 shows contour maps of the peak temperatures of spark kernels produced at pressures ranging from 300 to 1000 mbar. These peak temperatures are the 90th percentile of the path-averaged temperatures, meaning that the temperatures shown are hotter than 90% of the temperatures at a location. Peak temperatures were observed within the upper lobe of the kernels near z/D=1.1 and r/D=0.4 for all pressures. As with the initial time-resolved temperatures, the moderate-pressure kernels had the highest peak temperatures, followed closely by the atmospheric-pressure kernels and then the low-pressure kernels. The peak temperatures were 2070, 2490, and 2360 K at 380, 750, and 1000 mbar respectively. The lowest peak temperatures at the kernel edges were hotter at lower pressures, indicating greater uniformity of the peak temperature at lower pressure. This was again similar to the initial time-resolved average temperatures. The lowest peak temperatures were located at the furthest location that kernels were detected, and were 1000, 830, and 800 K at 380, 750, and 1000 mbar respectively. These results are consistent with the cause of the pressure dependence discussed in Section 4.2.2.

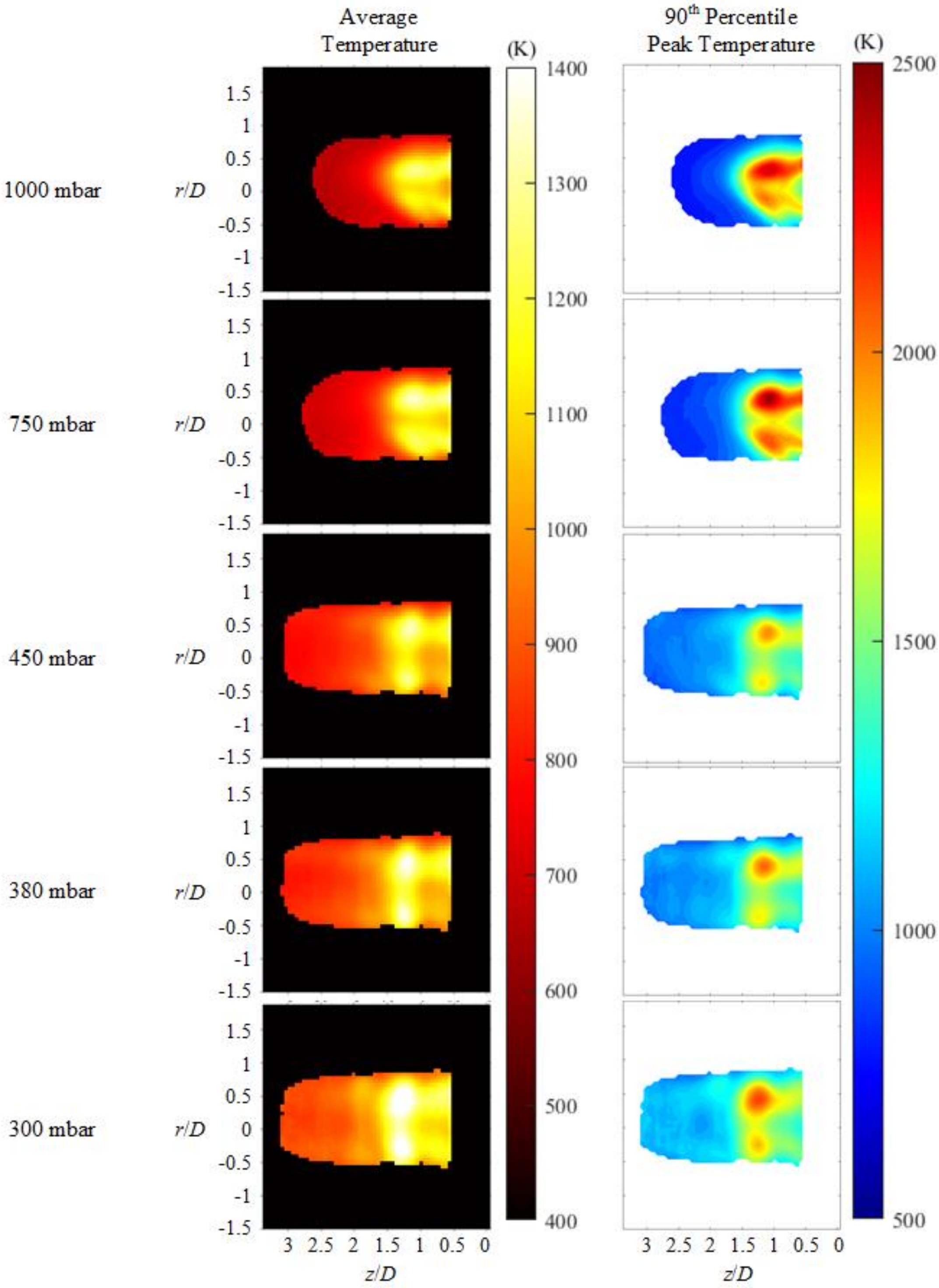

Figure 27 Time averaged temperature distributions (left) and 90th percentile temperature contour maps (right) for all kernels at pressures ranging from 300 to 1000 mbar.

4.2.4 Average Kernel Temperature Evolution

The temperature evolution of nonreacting spark kernels can serve as a baseline for comparison with spark kernels in combustible mixtures. Since there is no fuel to release heat, spark kernels in air decrease in temperature and will eventually approach the ambient air temperature. In a combustible mixture, the initial high plasma temperatures decrease within 1 ms [3]. If ignition is successful spark kernel temperature will approach the flame temperature for the mixture as heat from combustion is released into the kernel. If ignition is unsuccessful, spark kernel temperature will decrease and approach the ambient mixture temperature. Comparing the temperature evolution of failed ignition attempts to the temperature evolution of non-reacting spark kernels can be useful for estimating the amount of heat released by combustion reactions within the kernel. Figure 28 shows the evolution of the average non-reacting spark kernel temperatures. Average kernel temperatures reported are the volumetric average temperature of the kernels determined using the process described in Section 3.3.6.

Lower-pressure kernels were observed to be hotter on average than atmospheric-pressure kernels. Kernels were initially (i.e. 0.67 ms after plasma) 1280, 1190, and 1130 K at 380, 750, and 1000 mbar respectively. From 0.67 to 3.33 ms, average kernel temperatures decreased; kernels at the lowest pressures had the highest average temperatures. The rate of temperature decrease slowed between 0.67 and 3.33 ms; the average temperature then increased between 3.33 and 4 ms. The increase in energy from 3.33 to 4 ms is interesting as no energy was added to heat the gas in the kernels. Although it is not possible that the gas temperature increased without any added energy, it is possible that the average temperature increased, as alluded to with the increase in path-averaged temperature of the representative low-pressure kernel in Section 4.2.1. As cooler regions of the kernels continue to cool, they cease to emit enough radiation to be detected, and are no longer included when calculating the average kernel temperature. This is alluded to by the volume decrease in 4.1.3. The hotter regions were cooling at the same time that the volume was decreasing, so for the average temperature to increase the cooler gases must have reduced their emissions at a higher rate than the hotter gases were cooling.

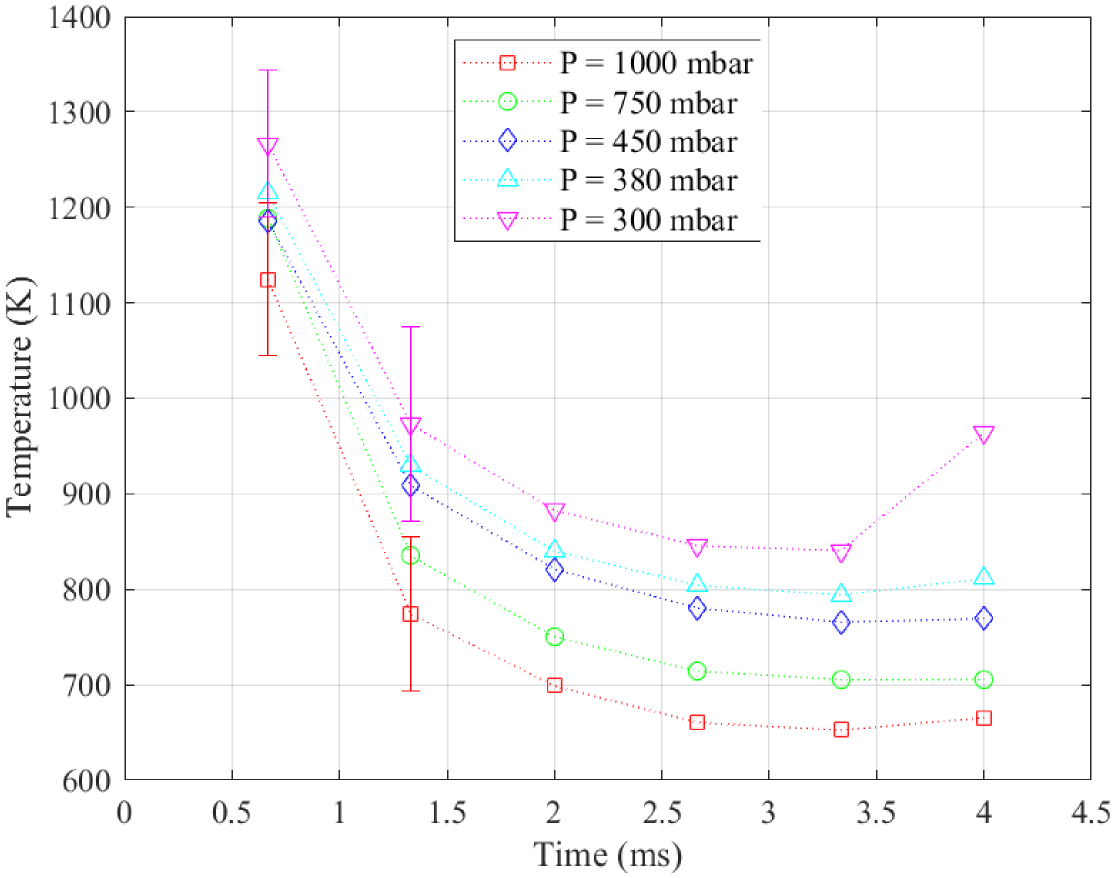

Figure 28 Spark kernel temperature evolution at pressures from 1000 to 380 mbar. Error bars represent systematic and precision uncertainty.

To identify the relative changes in kernel temperature at different subatmospheric pressures, the average kernel temperatures were normalized by their respective initial temperatures as shown in Figure 29. While it may seem like the atmospheric- and moderate-pressure kernels, being closer in temperature to their surroundings, would decrease in temperature at a lower rate than the low-pressure kernels, the opposite occurred. From 0.67 to 1.33 ms, the average temperature of kernels at atmospheric and moderate pressure decreased by roughly 30%, while low-pressure kernels (i.e. 300-450 mbar) decreased by roughly 23% over the same time. The faster rate of temperature decrease at atmospheric and moderate pressure is attributed to higher peak temperatures at these pressures transferring heat to their surroundings at a faster rate than at low pressures. The faster rate of cooling is attributed to greater availability of cool ambient air for entrainment and mixing due to greater density at higher pressure.

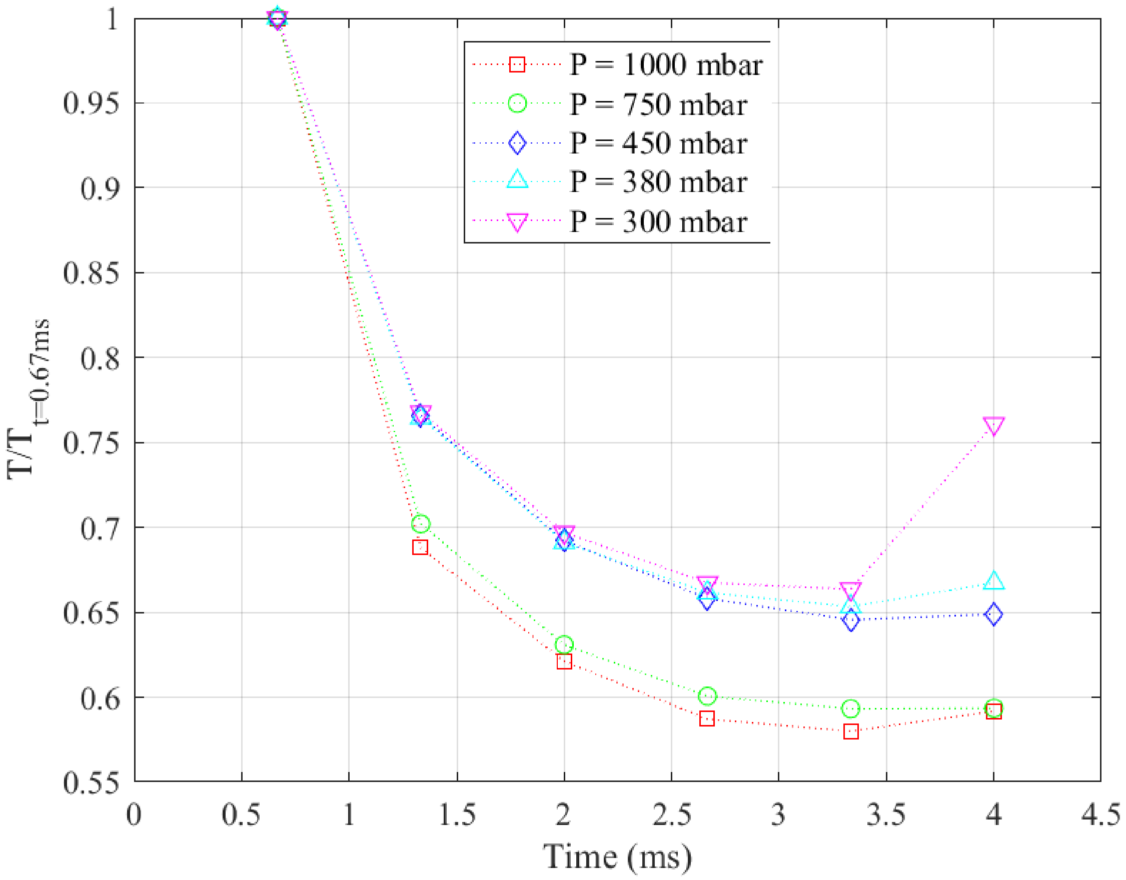

Figure 29 Kernel temperature evolution normalized by the initial temperature at 0.67 ms at each pressure.

4.3 Energy Results

Figure 30 shows the initial sensible energy in the kernels, the corresponding electrical energy deposited to the igniter, and the efficiency of conversion from electrical energy to sensible energy. Initially, kernels had between 0.25 J and 0.81 J of sensible energy, with the highest-pressure kernels containing the most energy, and the lowest-pressure kernels containing the least energy. Deposited electrical energy, based on measurements performed by collaborators at the Air Force Research Laboratory using the exciter and igniter used in this work, ranged from 0.85 J at 300 mbar to 1.02 J at 1000 mbar. Both the initial sensible energy and the deposited electrical energy decreased approximately linearly with decreasing pressure, but the sensible energy was more sensitive to pressure than electrical energy by a factor of 3. This means that the energy conversion efficiency was also pressure dependent, and ranged from approximately 30% at 300 mbar to 80% at atmospheric pressure.

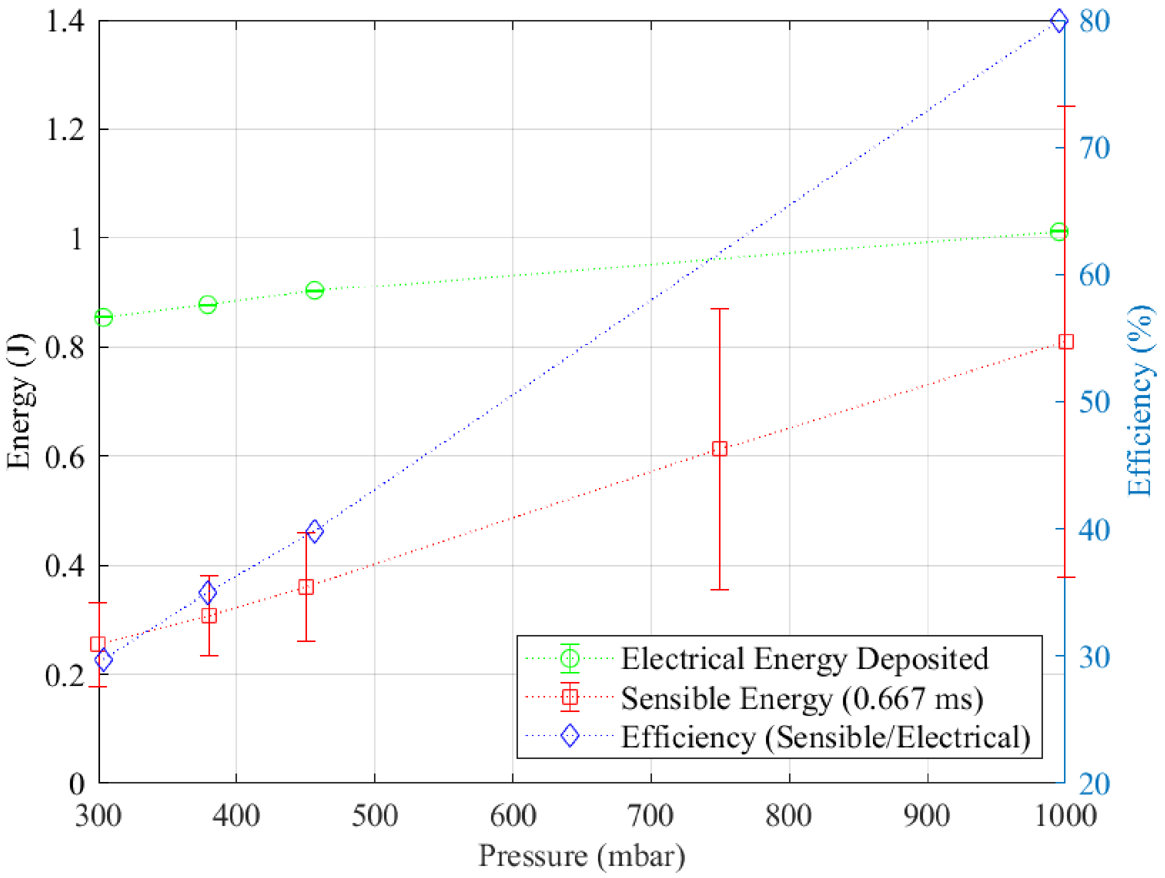

Figure 30 Comparison between deposited electrical energy, initial sensible energy, and electrical to sensible energy conversion efficiency. Error bars represent systematic and precision uncertainty.

The pressure dependence of both the energy deposition and the conversion efficiency may be explained by changes in the breakdown voltage of air. The breakdown voltage of air decreased along with pressure over the range observed [10,39]. Since the spark circuit used is passively triggered when the breakdown voltage is reached [35], lower breakdown voltages may mean that the exciter had less stored energy when the spark occurred. The decreased breakdown voltage could have also led to higher current in the spark channel and through the electrodes [18]. This increased current could have caused greater heating of the electrodes, representing an increased heat loss at lower pressures. Increased heating of the electrodes is anecdotally evidenced by the increased rate of ablation observed at lower pressures. The decrease in both electrical energy deposition and conversion efficiency may help explain some of the challenge with ignition at sub-atmospheric pressures since a decrease in either of these would decrease the energy delivered to the combustible mixture.

Chapter 5 Summary and Conclusions

In summary, a sunken fire type gas turbine igniter was used to produce spark kernels in air inside a pressure vessel. An infrared camera was used to measure the radiation intensity emitted by the kernels at atmospheric and sub-atmospheric pressures. An inverse deconvolution technique was employed to determine temperature distributions within the kernels, based on the infrared radiation emissions. The validity of the inverse deconvolution technique was evaluated using a laminar flat flame calibration burner, with agreement between deconvoluted and measured temperatures within 3%. The technique was analyzed to determine the sensitivity of the temperatures to the radiation model's inputs. The line-of-sight path length and pressure were the most influential parameters, both with a 15% increase in temperature for a 25% decrease in path length or pressure. Insights into the spatial development of spark kernels were reported, along with kernel temperature distributions and peak temperatures. The sensible energy contained within the kernels was determined from the kernel temperatures. The electrical energy deposited to the igniter was measured using an oscilloscope, high voltage probe, and current monitor, and compared with the calculated sensible energy.

The specific conclusions from this research are as follows.

I. Decreasing the ambient pressure causes a decrease in the peak temperatures within spark kernels. The 90th percentile temperature at 1000 mbar was 2370 K, while at 380 mbar the 90th percentile temperature was 2070 K. This change is attributed to changes in the spark characteristics at decreasing pressure. The reduction in peak temperatures of kernels can help to explain some of the challenge with high altitude ignition; successful ignition is dependent on obtaining sufficient temperatures.

II. The temperature distribution within spark kernels is more uniform at lower pressures. For example, the detectable kernel temperature distributions 0.67 ms after plasma ranged from 550 to 2050 K at atmospheric pressure, while at 380 mbar the temperature ranged from 750 to 1800 K. As with the trend in peak temperatures, this trend can be explained by changes in the spark discharge characteristics with decreasing pressure.

III. Average kernel temperatures increase with decreasing the ambient pressure, in contrast to the pressure sensitivity to peak kernel temperatures. The average kernel temperature 0.67 ms after plasma was detected was 1125 and 1270 K at 1000 and 300 mbar, respectively. The greater average temperatures at lower pressure occurs because the ratio of energy deposition to mass is higher at lower pressures.

IV. The efficiency of energy conversion from electrical to sensible energy decreases with decreasing pressure. Conversion efficiency at atmospheric pressure is estimated to be 80%, and decreases to 30% at 300 mbar. This is attributed to increased heat loss to the electrodes due to lower breakdown voltage of air at decreased pressures causing higher electrical current through the electrodes. This finding is significant because it can help to explain part of the challenge with achieving ignition at higher altitude.

V. Spark kernel volume is independent of pressure. This is attributed to the igniter diameter being fixed.

VI. Spark kernels travel faster and further from the igniter as pressure is reduced. For example, within 4 ms after plasma was detected, kernels at atmospheric pressure were detected 3 igniter diameters from the igniter tip, while at 300 mbar kernels were detected at least 3.4 diameters from the igniter tip. This observation is potentially significant because the fuel-air mixture within combustors is not homogenous, hence the placement of the spark kernel within the flow is an important design consideration.

It is anticipated that the results of this work can be used by engine designers when designing combustors or augmenters for high altitude ignition. Information about the temperature distribution of spark kernels can help guide designers in igniter placement within a combustion system, to ensure the hottest regions of spark kernels are created in a region where local conditions can support ignition. These results can also be used to validate a numerical model of ignition, if such a model were to be created.

Chapter 6 Future Work

Several avenues have been considered to better understand ignition at high altitude. In addition to low pressure, ignition at high altitude can also be challenging due to both low ambient temperature and water vapor dilution when attempting ignition in adverse weather conditions. Applying the technique described in this work to the impacts of ambient temperature and water vapor concentration on spark kernel temperatures could provide further insights into the ignition process at high altitude. Elucidating the combined effects of pressure, ambient temperature, water dilution, crossflow velocity (previous work by Okhovat), and turbulence intensity would then be logical next steps. Augmenters are downstream of the combustor and therefore require successful ignition in the presence of combustion products; measuring the effects of dilution with combustion products on the temperature of spark kernels could be valuable for augmenter design for ignition at all altitudes.

There is also opportunity to modify the experimental approach to investigate different aspects of spark kernels. Improvements to the spark discharge system could be made to allow for additional spark discharge characteristics to be investigated. Careful modifications to the resistance of the existing circuitry could be made to reduce the delivered energy, allowing for the combined impacts of delivered energy and sub-atmospheric pressure to be interrogated. The production igniter could be replaced with the more often studied opposed electrodes, allowing for the impact of electrode geometry and spark gap on the temperature distribution of spark kernels to be illuminated. These improvements would allow for more ready comparison with and expansion of results obtained using other techniques.

The present work optimized the camera settings to maximize framerate at the expense of resolution in order to obtain temperatures at known times after plasma. The technique could be modified to collect data at a slower framerate and higher resolution in order to capture more detailed temperature data. Under this premise, obtaining temperatures at known times would not be possible, however all images that do not contain plasma could be processed and greater detail could be provided for the spatial temperature distributions regardless of time after plasma. With some major modifications to the approach, it may be possible to determine radial temperature distributions within spark kernels. Modeling the kernels as stacks of circular slices, rather than elliptical slices as done in this work, would allow for the inverse Abel transform to be applied. Radial temperature profiles determined using the inverse Abel transform could provide better approximations of the maximum kernel temperatures than line-of-sight path averaged temperatures, which are influenced by cooler gases around and within the kernel vortices.

Finally, the igniter characterized in this work could be used to determine the minimum ignition energy of well-studied fuels. Relating the temperature distributions determined in this work to ignition energy could be used to help elucidate the underlying physics controlling ignition. With knowledge of the impact of temperature distribution on ignition energy, it may be possible to optimize the energy distribution produced by ignition systems to maximize ignition success.

Bibliography

[1] Lefebvre, A. H., and Ballal, D. R. *Gas Turbine Combustion: Altertative Fuels and Emissions*. Taylor & Francis, Boca Raton, FL, 2010.

[2] Buckmaster, J., Clavin, P., Liñán, A., Matalon, M., Peters, N., Sivashinsky, G., and Williams, F. A. "Combustion Theory and Modeling." *Proceedings of the Combustion Institute*, Vol. 30, No. 1, 2005, pp. 1–19. https://doi.org/10.1016/j.proci.2004.08.280.

[3] Mosbach, T., Gebel, G. C., Le Clercq, P., Sadr, R., Kannaiyan, K., and Al-Sharshani, A. Investigation of GTL-Like Jet Fuel Composition on GT Engine Altitude Ignition and Combustion Performance: Part II—Detailed Diagnostics. 2011.

[4] Fyffe, D., Moran, J., Kannaiyan, K., Sadr, R., and Al-Sharshani, A. Effect of GTL-Like Jet Fuel Composition on GT Engine Altitude Ignition Performance: Part I - Combustor Operability. 2011.

[5] Rosenker, M. V. *National Transportation Safety Board*. Washington, D.C., 2015.

[6] NTSC. *Aircraft Accident Report PT. Garuda Indonesia GA421, B737-300*. 2002.

[7] Neal, C. A., Casadevall, T. J., Miller, T. P., Hendley, J. W. I., and Stauffer, P. H. Volcanic Ash-Danger to Aircraft in the North Pacific. *USGS Fact Sheet 030-97*. https://pubs.usgs.gov/fs/fs030-97/fs030-97.pdf. Accessed Dec. 6, 2019.

[8] Lovett, J., Brogan, T., Philippona, D., Kiel, B., and Thompson, T. Development Needs for Advanced Afterburner Designs. 2004.

[9] Turns, S. R. *An Introduction to Combustion: Concepts and Applications*. McGraw-Hill, New York, 2000.

[10] Peek, F. W. "The Law of Corona and the Dielectric Strength of Air-II." *Proceedings of the American Institute of Electrical Engineers*, Vol. XXXI, No. 7, 1911, pp. 1051–1092. https://doi.org/10.1109/PAIEE.1911.6659605.

[11] Reinmann, R., and Akram, M. "Temporal Investigation of a Fast Spark Discharge in Chemically Inert Gases." *Journal of Physics D: Applied Physics*, Vol. 30, No. 7, 1997, p. 1125. https://doi.org/10.1088/0022-3727/30/7/010.

[12] Kono, M., Niu, K., Tsukamoto, T., and Ujiie, Y. "Mechanism of Flame Kernel Formation Produced by Short Duration Sparks." *Symposium (International) on Combustion*, Vol. 22, 1988, pp. 1643–1649.

[13] Borghese, A., Alessio, A. D., Diana, M., Venitozzi, C., and Motori, I. "Development of Hot Nitrogen Kernel Produced by a Very Fast Spark Discharge." *Symposium (International) on Combustion*, No. 22, 1988, pp. 1651–1659.

[14] Sforzo, B., Lambert, A., and Jagoda, J. "High Energy Spark Kernel Evolution : Measurements and Modeling." 2013, pp. 1–15.

[15] Sforzo, B., Lambert, A., Kim, J., Jagoda, J., Menon, S., and Seitzman, J. "Post Discharge Evolution of a Spark Igniter Kernel." *Combustion and Flame*, Vol. 162, No. 1, 2015, pp. 181–190. https://doi.org/10.1016/j.combustflame.2014.07.024.

[16] Okhovat, S., Hauth, J., and Blunck, D. "Temperatures of Spark Kernels Discharging into Quiescent or Cross-Flow Conditions." *Journal of Thermophysics and Heat Transfer*, Vol. 31, No. 1, 2017, pp. 120–129. https://doi.org/10.2514/1.T4927.

[17] Blunck, D. L., Kiel, B. V., Goss, L., and Lynch, A. "Spatial Development and Temperature of Spark Kernels Exiting into Quiescent Air." *Journal of Propulsion and Power*, Vol. 28, No. 3, 2012, pp. 458–465. https://doi.org/10.2514/1.B34131.

[18] Dale, J., Checkel, M. D., and Smy, P. R. "Application of High Energy Ignition Systems to

Engines." *Progress in Energy and Combustion Science*, Vol. 23, Nos. 5–6, 1997, pp. 379–398. https://doi.org/10.1016/S0360-1285(97)00011-7.

[19] EASA. "Certification Specifications for Engines." No. Amendment 3, 2010, pp. 1–166.

[20] Shepherd, J. E., and Lee, J. J. "Spark Ignition Energy Measurements in Jet A, NTSB Report." 2000, p. 87.

[21] Bane, S. P. M., Ziegler, J. L., Boettcher, P. A., Coronel, S. A., and Shepherd, J. E. "Experimental Investigation of Spark Ignition Energy in Kerosene, Hexane, and Hydrogen." *Journal of Loss Prevention in the Process Industries*, Vol. 26, No. 2, 2013, pp. 290–294. https://doi.org/10.1016/j.jlp.2011.03.007.

[22] Shepherd, J. E., Krok, J. C., and Lee, J. J. "Spark Ignition Energy Measurements in Jet A." 2000, p. 87.

[23] Lee, T. W., Jain, V., and Kozola, S. "Measurements of Minimum Ignition Energy by Using Laser Sparks for Hydrocarbon Fuels in Air: Propane, Dodecane, and Jet-A Fuel." *Combustion and Flame*, Vol. 125, No. 4, 2001, pp. 1320–1328. https://doi.org/10.1016/S0010-2180(01)00248-6.

[24] Moorhouse, J., Williams, A., and Maddison, T. E. "Investigation of the Minimum Ignition Energies of Some C1 to C7 Hydrocarbons." *Combustion and Flame*, Vol. 23, 1974, pp. 203–213.

[25] Eckhoff, R. K., Ngo, M., and Olsen, W. "On the Minimum Ignition Energy (MIE) for Propane/Air." *Journal of Hazardous Materials*, Vol. 175, Nos. 1–3, 2010, pp. 293–297. https://doi.org/10.1016/j.jhazmat.2009.09.162.

[26] Ballal, D. R., and Lefebvre, A. H. A General Model of Spark Ignition for Gaseous and Liquid Fuel-Air Mixtures. 1981.

[27] Zhang, W., Gou, X., and Chen, Z. "Effects of Water Vapor Dilution on the Minimum Ignition Energy of Methane, n-Butane and n-Decane at Normal and Reduced Pressures." *Fuel*, Vol. 187, 2017, pp. 111–116. https://doi.org/10.1016/j.fuel.2016.09.057.

[28] Ballal, D. R., and Lefebvre, A. H. "The Influence of Flow Parameters on Minimum Ignition Energy and Quenching Distance." *Symposium (International) on Combustion*, Vol. 15, No. 1, 1975, pp. 1473–1481.

[29] Ono, R., Nifuku, M., Fujiwara, S., Horiguchi, S., and Oda, T. "Minimum Ignition Energy of Hydrogen-Air Mixture: Effects of Humidity and Spark Duration." *Journal of Electrostatics*, Vol. 65, No. 2, 2007, pp. 87–93. https://doi.org/10.1016/j.elstat.2006.07.004.

[30] Okhovat, S. *Temperature Evolution of Spark Kernels in Quiescent and Cross-Flow Conditions*. Oregon State University, 2015.

[31] Kuchta, J. M. *SUMMARY OF IGNITION PROPERTIES SOF JET FUELS AND OTHER AIRCRAFT ~COMBUSTIBLE FLUIDS*. Wright Patterson Air Force Base, Ohio, 1975.

[32] Sforzo, B., Kim, J., Jagoda, J., and Seitzman, J. "Ignition Probability in a Stratified Turbulent Flow with a Sunken Fire Igniter." *Journal of Engineering for Gas Turbines and Power*, Vol. 137, No. 1, 2015. https://doi.org/10.1115/1.4028208.

[33] Topham, D. R., Clements, R. M., and Smy, P. R. "Turbulent Mixing in a Pulsed Plasma-Jet Exhaust." *Journal of Fluid Mechanics*, Vol. 148, No. 1, 1984, pp. 207–224.

[34] Blunck, D., and Kiel, B. V. *Trajectory, Development, and Temperature of Spark Kernels Exiting into Quiescent Air*. Dayton, OH, 2012.

[35] Ignition Systems for Turbines. *Champion Aerospace*.

[36] Ko, Y., Anderson, R. W., and Arpaci, V. S. "Spark Ignition of Propane-Air Mixtures Near

the Minimim Ignition Energy: Part I. An Experimental Study." *Combustion and Flame*, Vol. 83, No. 1, 1991, pp. 75–87.

[37] Ballal, D. R., and Lefebvre, A. H. "The Influence of Spark Discharge Characteristics on Minimum Ignition Energy in Flowing Gases." *Combustion and Flame*, Vol. 24, 1975, pp. 99–108.

[38] Fridman, A., and Kennedy, L. A. *Plasma Physics and Engineering*. CRC Press, Boca Raton, FL, 2011.

[39] Pedersen, A. "Calculation of Spark Breakdown or Corona Starting Voltages in Nonuniform Fields." *IEEE Transactions on Power Apparatus and Systems*, Vol. PAS-86, No. 2, 1967, pp. 200–206. https://doi.org/10.1109/TPAS.1967.291836.

[40] Raizer, Y. P. *Gas Discharge Physics*. Springer-Verlag, New York, 1991.

[41] Au, S., Haley, R., and SMY, P. R. "The Influence of the Igniter-Induced Blast Wave Upon the Initial Volume and Expansion of the Flame Kernel." *Combustion and Flame*, Vol. 88, No. 1, 1992, pp. 50–60.

[42] Grosshandler, W. L. RADCAL: A Narrow-Band Model for Radiation Calculations in a Combustion Environment. http://nvlpubs.nist.gov/nistpubs/Legacy/TN/nbstechnicalnote1402.pdf.

[43] Migliorini, F., De Iuliis, S., Cignoli, F., and Zizak, G. "How 'Flat' Is the Rich Premixed Flame Produced by Your McKenna Burner?" *Combustion and Flame*, Vol. 153, No. 3, 2008, pp. 384–393. https://doi.org/10.1016/j.combustflame.2008.01.007.

[44] Stamatoglou, P. *Spectral Analysis of Flame Emission for Optimization of Combustion Devices on Marine Vessels*. Lund University, 2014.

[45] Gordon, S., and McBride, B. J. Computer Program for Calculation of Complex Chemical Equilibrium Compositions and Applications II. User's Manual and Program Description. http://www.grc.nasa.gov/WWW/CEAWeb/RP-1311P2.htm.

[46] Hindasageri, V., Vedula, R. P., and Prabhu, S. V. "Thermocouple Error Correction for Measuring the Flame Temperature with Determination of Emissivity and Heat Transfer Coefficient." *Review of Scientific Instruments*, Vol. 84, No. 2, 2013. https://doi.org/10.1063/1.4790471.

[47] Figliola, R. S., and Beasley, D. E. *Theory and Design for Mechanical Measurements*. John Wiley & Sons, Inc., 2006.

[48] Shariff, K., and Leonard, A. "Vortex Rings." *Annu. Rev. Fluid Mech*, Vol. 24, 1992, pp. 235–79. https://doi.org/10.1146/annurev.fl.24.010192.001315.

[49] Srivastava, D. K., and Agarwal, A. K. "Comparative Experimental Evaluation of Performance, Combustion and Emissions of Laser Ignition with Conventional Spark Plug in a Compressed Natural Gas Fuelled Single Cylinder Engine." *Fuel*, Vol. 123, 2014, pp. 113–122. https://doi.org/10.1016/j.fuel.2014.01.046.

[50] Rumble, J. R. *CRC Handbook of Chemistry and Physics, 100th Edition (Internet Version 2019)*. CRC Press/Taylor & Francis, Boca Raton, FL.

APPENDICIES

Appendix A: Spectral Response Profiles

Spectral transmission profile for the sapphire window:

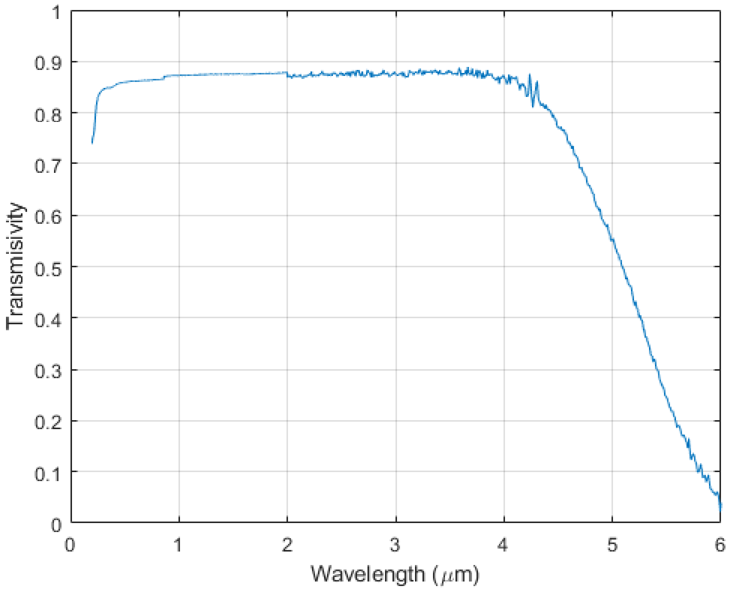

Spectral transmission profile for the camera lens:

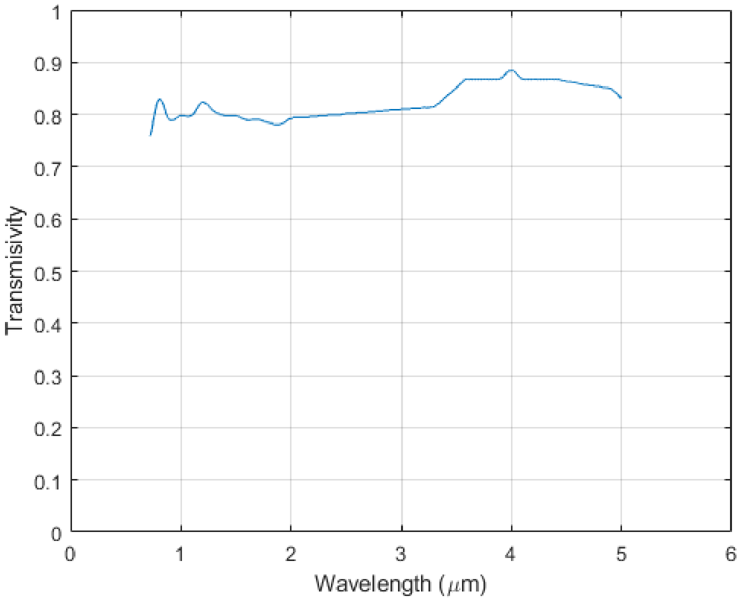

Spectral response profile for the camera detector:

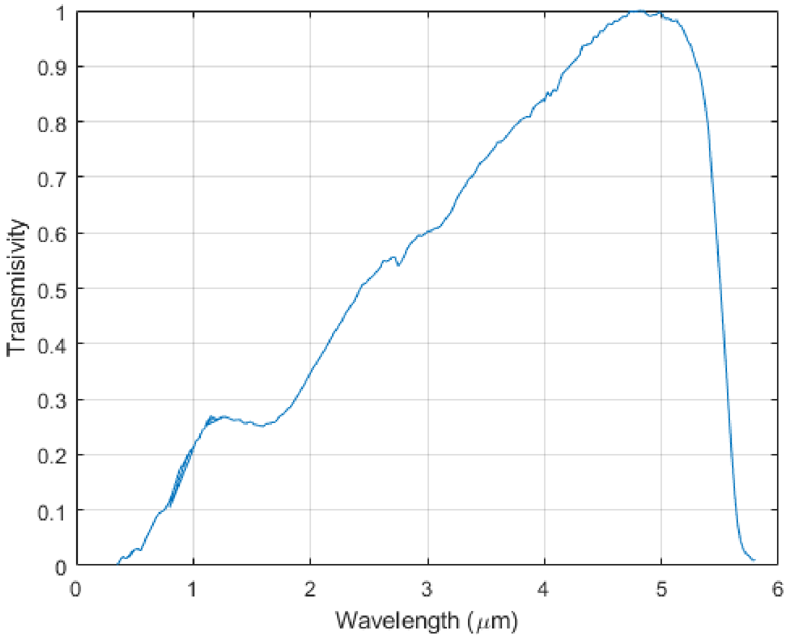

Example of the spectral intensity calculated using RADCAL, convolved with the transmission profiles of the window, lens, and detector:

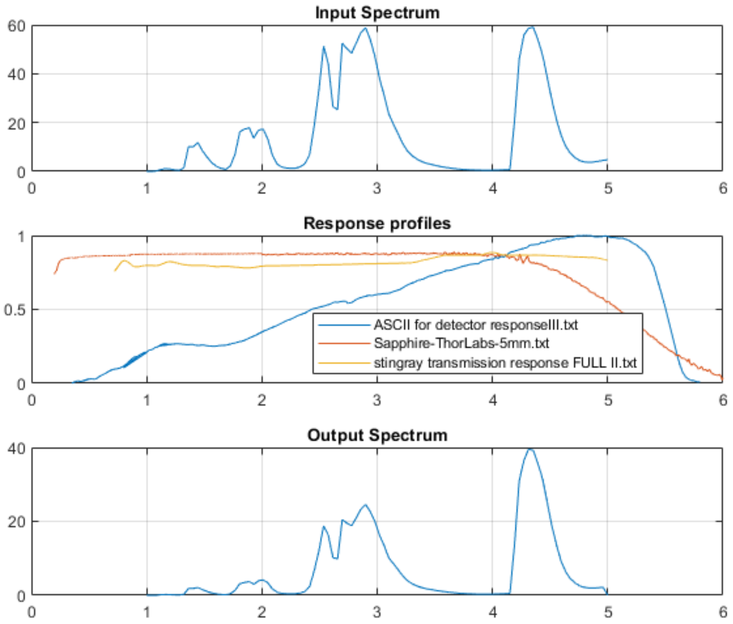

Appendix B: Air Composition Analysis

RADCAL requires the partial pressures of H_2O, CO_2, N_2, CH_4, and O_2 as inputs when calculating the spectral emissions from the gas. The mole fraction of H_2O was determined using psychrometric calculations based on the measured ambient pressure, temperature, and relative humidity in the room. The mole fraction of CO_2 was directly. It was assumed that the concentration of CH_4 was negligible since no fuel was present. The mole fractions of O_2 and Ar were taken to be 0.2095 and 0.0093, respectively, based on Handbook of Chemistry and Physics values [50]. The mole fraction of N_2 was then taken to be the remainder assuming that all mole fractions added to unity. Assuming ideal gas behavior, the mole fractions of each gas was multiplied by the absolute pressure in the vacuum chamber to get the partial pressures required by RADCAL.

Appendix C: Uncertainty Analysis

Details of the sources of error considered for each measurement are listed in the bulleted list below. Uncertainties at the same bullet levels were combined using the sum of their squares [47]. Uncertainties were estimated at 95% confidence.

Temperature Uncertainty:

- RSS combination of the sequential perturbation of RADCAL to each input:
    - Intensity: ±0.99-3.53 W/m^2-sr-µm through detector dynamic range
        - Calibration curve fit correlating photon count to integrated intensity: ±1.91x10^{-14} W/m^2-sr-µm
        - Photon counts (sequential perturbation of curve fit to determine sensitivity to uncertainty of photon count): ±1.31 W/m^2-sr-µm
            - Camera Accuracy: ±1% (photon count) (mfg)
            - Statistical error in measured photon count: ±0.5-2.2% through detector dynamic range
        - Blackbody calibration source (sequential perturbation of convolved and integrated blackbody emission spectrum): ±0.84 W/m^2-sr-µm
            - Emissivity: ±0.01 (mfg)
            - Temperature: ±1.17-1.37 °C on temperature range used
                - Resolution: ±1°C (mfg)
                - Uniformity: ± 0.5 to 3 °C (mfg) (assumed linear through temperature range)
                - Stability: ±0.25°C (mfg)
    - Pressure: ±11 mbar
        - Transducer: ±3.7 mbar
            - Accuracy: ±0.05% span (mfg)
            - Repeatability: ±0.02% span (mfg)
        - Vacuum chamber pressure stability
            - ±10 mbar (anecdotal)
    - CO_2 concentration: ±11.4 ppm
        - Instrument error: ±35.2 ppm
            - Static accuracy: ±30 ppm (mfg)
            - Dynamic accuracy: ±3% measurement (mfg)
            - Repeatability: ±10 ppm (mfg)
        - Statistical error (combined across all test days): ±11.4 ppm
    - H_2O concentration ± 2.18 ppt
        - Instrument error ±1.33 RH
            - Accuracy: ±3% RH (mfg)
            - Repeatability: ±0.1% RH (mfg)
        - Statistical error (combined across all test days): ±6.7 RH
    - Pathlength: ±1.19mm on average across pressures

        - Edge detection resolution: ±0.51mm/pixel
            - Pixel resolution: 0.64 mm/pixel (1/2 resolution used)
            - Spatial calibration source resolution: 0.8 mm (1/2 resolution used)
            - Both resolutions were counted twice due to two edge detections per pathlength
        - Pathlength sensitivity to edge detection threshold (Sequential perturbation with 4±1 standard deviations above average background noise.): ±0.72mm on average across pressures
- Statistical error in the deconvoluted temperatures: dependent on pixel data.

Error sources not considered:

- Error contributions due to the RADCAL model
- Interpolation database (expected to be negligible)
- Uncertainty of the optical spectral transmission profiles
- CO_2 calibration source (expected to be negligible)